Modelling supernova line profile asymmetries to determine ejecta dust masses: SN 1987A from days 714 to 3604

Antonia Bevan[1] and M. J. Barlow[1]

[1]*Department of Physics and Astronomy, University College London, Gower Street, London WC1E 6BT, UK*

ABSTRACT

The late time optical and near-IR line profiles of many core-collapse supernovae exhibit a red-blue asymmetry as a result of greater extinction by internal dust of radiation emitted from the receding parts of the supernova ejecta. We present here a new code, DAMOCLES, that models the effects of dust on the line profiles of core-collapse supernovae in order to determine newly formed dust masses. We find that late-time dust-affected line profiles may exhibit an extended red scattering wing (as noted by Lucy et al. (1989)) and that they need not be flux-biased towards the blue, although the profile peak will always be blueshifted. We have collated optical spectra of SN 1987A from a variety of archival sources and have modelled the Hα line from days 714 to 3604 and the [O I] 6300,6363 Å doublet between days 714 and 1478. Our line profile fits rule out day 714 dust masses $> 3 \times 10^{-3}$ M$_\odot$ for all grain types apart from pure magnesium silicates, for which no more than 0.07 M$_\odot$ can be accommodated. Large grain radii ($\geqslant 0.6$ μm) are generally required to fit the line profiles even at the earlier epochs. We find that a large dust mass (≥ 0.1 M$_\odot$) had formed by day 3604 and infer that the majority of the present dust mass must have formed after this epoch. Our findings agree with recent estimates from spectral energy distribution fits for the dust mass evolution of SN 1987A and support the inference that the majority of SN 1987A's dust formed many years after the initial explosion.

Key words: radiative transfer – supernovae: general – supernovae: individual: SN 1987A – ISM: supernova remnants.

1 INTRODUCTION

Core-collapse supernovae (CCSNe) have long been thought to be potential dust factories (Hoyle & Wickramasinghe 1970; Kozasa et al. 1991; Todini & Ferrara 2001). However over the previous decade observations at mid-infrared (mid-IR) wavelengths of warm dust emission from CCSNe had suggested that the quantities of dust produced, typically $\leq 10^{-3}$ M$_\odot$ during the first 1000 d (Sugerman et al. 2006; Meikle et al. 2007; Kotak et al. 2009; Andrews et al. 2010; Fabbri et al. 2011) were much less than the 0.1-1.0 M$_\odot$ of dust per CCSN estimated to be needed (Morgan & Edmunds 2003; Dwek et al. 2007) in order to account for the very large dust masses measured in some high redshift galaxies (Omont et al. 2001; Bertoldi et al. 2003; Watson et al. 2015). However, recent *Herschel* far-IR and sub-mm observations of cold dust masses as high as 0.2-0.8$M_\odot$ in several young supernova remnants have resulted in a re-evaluation of the rate of dust production by CCSNe (Barlow et al. 2010; Matsuura et al. 2011; Gomez et al. 2012). The *Hershel* dust mass estimates were based on fitting dust spectral energy distribu-

tions (SEDs) that peaked at far-IR wavelengths. Following the end of the *Herschel* mission in 2013 there is likely to be a long wait for far-IR facilities with comparable or better sensitivities than *Herschel* to become available, providing an incentive to make use of alternative methods to estimate the dust masses that form in supernova ejecta.

The absorption and scattering of optical or near-IR radiation by newly-formed dust within the ejecta of supernovae can result in an asymmetry between the red and blueshifted components, with redwards emission from the far side of the ejecta undergoing greater absorption. Lucy et al. (1989) identified a progressive blueshifting of the [O I] $\lambda\lambda$6300,6363 Å doublet from SN 1987A between days 529 and 739 after outburst, with the doublet in the later spectrum being blueshifted by ~ 600 km s^{-1}. Since then, such red-blue asymmetries have been frequently observed in the late-time (> 400 d) spectra of supernova ejecta and there is now a growing data base of such observations (e.g. Lucy et al. (1989); Fabbri et al. (2011); Mauerhan & Smith (2012); Milisavljevic et al. (2012)).

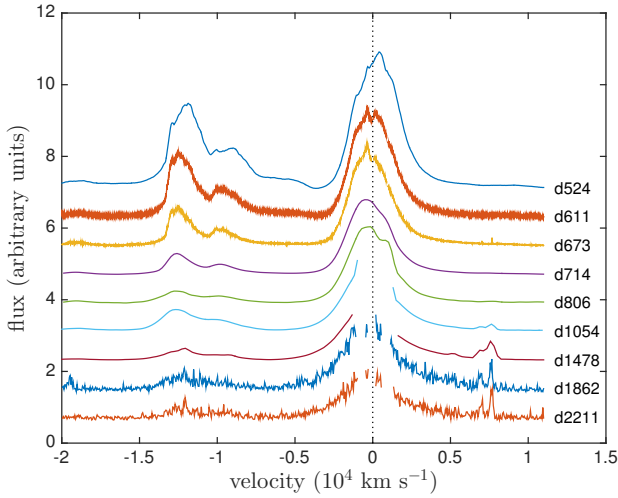SN 1987A as an archetypal object is critical to our grow-

Figure 1. Archival data showing the evolution of the Hα and [O I] line profiles from SN 1987A at the earlier of the epochs considered. The spectral gaps at the last two epochs correspond to where narrow line emission from the equatorial ring has been removed. The spectra have been continuum-subtracted and offsets have ben applied for display purposes.

Figure 2. Archival data showing the evolution of the Hα line profile from SN 1987A at the later epochs. The spectral gaps correspond to where narrow line emission from the equatorial ring has been removed. The spectra have been continuum-subtracted and offsets applied for display purposes.

ing understanding of the formation and evolution of dust in CCSNe. Since its outburst there have been numerous observations at many wavelengths and many epochs. Mid-infrared emission from warm dust (T∼400 K) was observed by day ∼450 (Roche et al. 1989; Bouchet et al. 1991; Wooden et al. 1993) and by day 775 the emitting dust mass was estimated to have been between $\sim 5 - 20 \times 10^{-4}$ M$_\odot$ (Wooden et al. 1993; Ercolano et al. 2007; Wesson et al. 2015). Beginning from 23 yr after outburst, the *Herschel Space Observatory* detected much larger quantities (0.4–0.8 M$_\odot$ of T∼20 K cold dust emitting at far-IR and submillimetre wavelengths (Matsuura et al. 2011, 2015). This emission has been confirmed by ALMA observations to originate from the ejecta of SN 1987A (Indebetouw et al. 2014).

We here seek to model the effects of dust on line profiles with a view to providing both an alternative way of determining dust masses formed in the ejecta of CCSNe and in order to investigate the effects of dust on the shapes of line profiles emitted from these objects. We present a new code, DAMOCLES (Dust Affected Models Of Characteristic Line Emission in Supernovae), that utilizes a Monte Carlo methodology in order to model line profiles in expanding atmospheres. The code can treat dust composed of multiple species and grain sizes with variable ejecta density and velocity distributions. Both clumped and smooth geometries may be modelled.

In this paper, we collate optical spectra from the archives of four different telescopes in order to study the effects of dust formation on the Hα line and on the [O I] λ6300,6363 Å doublet. We model epochs spanning a range of approximately 8 yrs from the first indications of blueshifting in the Hα line between days 600–700, using both smooth and clumped geometries. We compare our derived dust masses to those obtained by Wesson et al. (2015, hereafter 2015) and Dwek & Arendt (2015, hereafter DA15) and
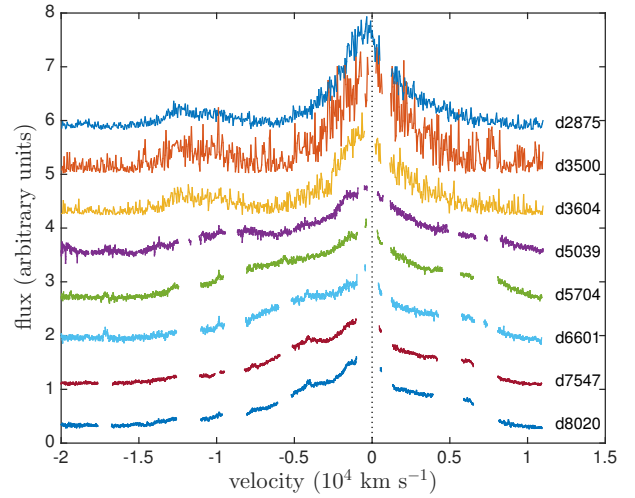
consider the implied dust formation rate. We present our testing of the new code against analytical cases and previously published optically thick models (Lucy et al. 1989). We also investigate the sensitivity of line profiles to each of the variables and note the range of signatures that observed line profiles may exhibit in the presence of dust.

In Section 2, we detail the observed spectra that we used for our modelling. In Section 3, we discuss the details of the DAMOCLES code and in Section 4 we present our testing of the code and our parameter sensitivity analyses. Our modelling of the Hα and [O I] λ6300,6363 Å lines is presented in Section 5 and we discuss our findings in Section 6.

2 ARCHIVAL SPECTRA OF SN 1987A

SN 1987A has been the most intensively observed supernova in history, with a wealth of both spectral and photometric data available to model. From the archives of a number of different telescopes we have collated optical spectra acquired over a wide range of epochs. At the earlier epochs we use spectra obtained by the Anglo-Australian Telescope (AAT) and the Cerro Tololo Inter-American Observatory (CTIO) and at later epochs we use spectra from the archives of the *Hubble Space Telescope* (*HST*) and the Very Large Telescope (VLT). An explosion date of 1987 February 23 is adopted throughout and epochs are measured relative to this date. Full details of all observations may be found in Table 1. The spectral resolutions of the grating spectrograph observations are listed in column 7, while column 8 lists the spectral resolving powers of the echelle spectrograph observations.

Wavelength ranges encompassing the Hα line and [O I] λλ6300,6363 Å doublet were selected in order to trace their evolution from day 524, near the time of the first indications of dust formation (Wooden et al. 1993), to day 8020,

Table 1. Details of the archival data for SN 1987A.

Date	Age (d)	Telescope	Inst	$\lambda_{\min}$ (Å)	$\lambda_{\max}$ (Å)	Res. (Å)	Res. Power	Reference
31 Jul 1988	524	AAT	FORS	5500	10190	20		Spyromilio et al. (1991)
26 Oct 1988	611	AAT	UCLES	6011	7336		30000	Hanuschik et al. (1993); Spyromilio et al. (1993)
27 Dec 1988	673	AAT	UCLES	5702	10190		30000	Hanuschik et al. (1993); Spyromilio et al. (1993)
06 Feb 1989	714	CTIO-1.5m	Cass.	6420	10380	16		Phillips et al. (1990)
09 May 1989	806	CTIO-1.5m	Cass.	6430	10330	16		Phillips et al. (1990)
12 Jan 1990	1054	CTIO-4m	RC	3565	10000	11		Suntzeff et al. (1991)
12 Mar 1991	1478	CTIO-4m	RC	3245	9175	11		
30 Mar 1992	1862	*HST*	STIS	4569	6818	4.4		Wang et al. (1996)
14 Mar 1993	2211	*HST*	STIS	4569	6818	4.4		Wang et al. (1996)
07 Jan 1995	2875	*HST*	STIS	4569	6818	4.4		Chugai et al. (1997)
23 Sep 1996	3500	*HST*	STIS	4569	6818	4.4		
05 Jan 1997	3604	*HST*	STIS	4569	6818	4.4		
10 Dec 2000	5039	VLT	UVES	4760	6840		50000	Gröningsson et al. (2006, 2007)
06 Oct 2002	5704	VLT	UVES	4760	6840		50000	Gröningsson et al. (2006, 2007, 2008)
21 Mar 2005	6601	VLT	UVES	4760	6840		50000	Gröningsson et al. (2006, 2007)
23 Oct 2007	7547	VLT	UVES	4760	6840		50000	Gröningsson et al. (2007)
07 Feb 2009	8020	VLT	UVES	4800	6800		50000	Tziamtzis et al. (2010)

near the current era. Optical spectroscopy obtained at the AAT using the Faint Object Red Spectrogaph (FORS) during the first 2 yr after outburst was kindly supplied by Dr Raylee Stathakis (Spyromilio et al. 1991; Hanuschik et al. 1993; Spyromilio et al. 1993) and optical spectra from the CTIO were donated by Dr Mark Phillips (Suntzeff et al. 1991).

The evolution of the Hα and [O I] line profiles is presented in Figs 1 and 2. At later epochs, the broad Hα profile emitted by the ejecta becomes contaminated by narrow line emission from the equatorial ring. These lines have been removed for the purposes of modelling the broad line. A continuum fit has been subtracted from each spectrum and a velocity correction has been applied for a recession velocity of 287 km s^{-1} (Gröningsson et al. 2008).

2.1 Contamination of the Hα profiles

The Hα profile at day 714 exhibits a very slight inflection visible at $V \approx +900$ km s^{-1}. By day 806, this slight inflection has developed into a noticeable shoulder in the line profile of Hα (see Fig. 11).

Although these features are similar in nature to features produced by dust absorption in the flat-topped region (as discussed in Section 4.3.5), we conclude that this shoulder is an early appearance of the unresolved [N II] λ6583 Å line from the equatorial ring (Kozma & Fransson 1998b). Unresolved nebular [N II] lines at $\lambda = 6583$ Å and $\lambda = 6548$ Å either side of the Hα rest-frame velocity at 6563 Å are certainly seen by day 1054 and have to be removed in order to consider the evolution of the broad Hα profile (see Fig. 1). We do not remove this potential contaminant at earlier epochs but try to fit the broad line profiles around it.

By day 1054, all three of the narrow nebular lines are strong. They remain unresolved in the low spectral resolution CTIO data at days 1054 and 1478 and therefore contaminate the entire central region of the Hα line profile. Their presence renders two CTIO Hα profiles from days 1054 and 1478 unusable for modelling purposes. The HST and VLT

Table 2. Hα FWHM and the HWZI determined by the zero intensity velocity on the blue side of the line. The tabulated line widths have been corrected for the relevant instrumental resolution.

day	FWHM (Å)	HWZI (Å)
524	3200	3600
611	2700	3400
673	1600	3700
714	3100	4500
806	3200	5500
1054	2100	5600
1478	1400	6600
1862	1600	6800
2211	1400	6700
2875	2700	6700
3500	3500	7000
3604	2100	7000

Hα profiles at later epochs (≥ 1862 d) have a higher spectral resolution and it was therefore easier to remove the narrower [N II] and Hα lines from the broad Hα profiles (for example Figs 1 and 2). Although this does remove a potentially informative section of the profile ($+500$ km s$^{-1} < v < +1500$ km s^{-1}), we achieve good fits to the overall line profiles at these epochs.

2.2 The evolution of the maximum and minimum velocities

For a freely expanding medium, the velocity of any fractional radial element should not change with time. The maximum velocity of any line-emitting region is therefore expected to be constant. However, at the epochs we consider here, it appears that the maximum velocities of the Hα line, as determined by the velocity at zero intensity on the blue side, generally increase over time (see Table 2). We attribute this to the start of the freeze-out phase in the outer regions of the ejecta, while the hydrogen neutral fraction is still increasing in the denser inner regions (Danziger et al. 1991; Fransson & Kozma 1993).

The onset of a fixed ionization structure in the ejecta causes the rate of Hα flux decline to slow. Since the outer, faster moving regions reach this state at earlier times than the inner, slower moving regions, the relative flux contribution of the outer regions is increased. At early epochs ($t < 900$ d) the flux contribution from hydrogen in the core dominates the overall Hα flux, whereas at later epochs ($t > 900$ d) the flux from the envelope dominates (Fransson & Kozma 1993; Kozma & Fransson 1998a). This shift likely explains apparent broadening of the line with the higher velocity material becoming increasingly noticeable in the line profiles. This may also explain the increase in half-width zero intensity (HWZI) velocities at these epochs with the relative flux from the very densest regions dropping more rapidly relative to the outer line-emitting region. The full width at half-maximum (FWHM) remains relatively steady (see Table 2). However, the FWHM values presented in Table 2 were difficult to determine accurately since the peak of the broad line profile is contaminated by narrow line emission from the equatorial ring.

3   THE DAMOCLES CODE

Monte Carlo methods have long been used to model radiative transfer problems in diverse environments and there are several examples of codes which apply the technique in application to supernovae (for example Maeda et al. (2003); Lucy (2005); Jerkstrand et al. (2012); Owen & Barlow (2015)). Whilst there are numerous codes that treat dust or gas or both in order to produce an overall SED, there is a dearth of codes designed to focus on the shapes of individual line profiles. Although a velocity field is naturally considered in codes that seek to reproduce the spectra of supernovae, absorption and scattering by dust is not and thus the resulting shapes of line profiles are potentially unrepresentative of those emerging from dusty ejecta at late times.

In this work we aim to model single or doublet line profiles produced by a moving atmosphere in a dusty medium. Since a comparatively small wavelength range is considered, a fully self-consistent radiative transfer model is unnecessarily expensive. Instead any energy packet that is absorbed during the simulation may simply be removed on the grounds that it would be reemitted outside the wavelength range of interest. This approach is clearly not applicable to SED radiative transfer models that treat continuum emission from dust. The extinction due to dust is assumed to be temperature-independent and it is therefore unnecessary to iteratively calculate the temperature of the ejecta as in a fully self-consistent calculation of the SED. Though clearly the total energy transferred through the medium is not conserved in the wavelength range of interest, the signature of the normalized line profile is preserved.

The DAMOCLES code builds on the work of Lucy et al. (1989) who employed a similar approach to model the broad [O I] λ6300,6363 Å doublet seen in SN 1987A at early epochs (up to ∼ day 775). It models the transport of initially monochromatic energy packets through a smooth or clumped dusty medium having a smooth velocity field. The velocity field and the inner and outer ejecta radii are free parameters. The late-time (> 400 d) line emission is assumed to be optically thin, with an emissivity distribution proportional to the square of the local gas density, i.e. proportional to the product of the recombining proton and electron densities in the case of Hα or to the product of the neutral oxygen and electron densities in the case of collisionally excited [O I] emission.

3.1   The energy packet formalism

The initial radiation field is inherently tied to the distribution of gas throughout the supernova ejecta which is declared as a power law $\rho(r) \propto r^{-\beta}$ between $R_{\rm in}$ and $R_{\rm out}$. $R_{\rm out}$ is calculated directly from the epoch of the line to be modelled and the declared maximum line velocity. The emissivity distribution is also specified as a power law with $i(\rho) \propto \rho^k$. However this is generally taken to be $i(r) \propto r^{-2\beta}$ since the majority of lines modelled are optically thin recombination lines or collisionally excited lines and therefore $i(\rho) \propto \rho^2$. The radiation is quantised into monochromatic packets with equal energy $E_0 = nh\nu_0$. In Monte Carlo simulations (that model non-moving media) packets are usually taken to be of constant energy. When the frequency of a packet is altered after an event, the energy of that packet is kept constant and the number of real photons contained within it is assumed to change. However, in the case of dust scattering, the number of real photons is conserved and thus the energy of the packet is altered. This is most easily achieved by weighting each packet over all scattering events as

$$w = \prod_{\rm scat} \frac{\nu'}{\nu} \qquad (1)$$

where w is the weight of the packet and ν and ν' are the frequencies of the packet before and after the scattering event respectively. The final energy of each packet is then $E = wE_0$, where E_0 is the initial energy of the packet.

The emissivity distribution is calculated by dividing the ejecta into a specifiable number of shells between $R_{\rm in}$ and $R_{\rm out}$ overlaid on the Cartesian grid and the number of packets to be emitted isotropically in each shell calculated according to the specified emissivity and density power laws. For each packet a location within that shell and an initial trajectory is randomly sampled from an isotropic distribution such that

$$\phi = 2\pi\eta \qquad (2)$$
$$\cos\theta = 2\xi - 1 \qquad (3)$$

where $0 < \eta < 1$ and $0 < \xi < 1$ are random numbers, ϕ is the azimuthal angle and $\cos\theta$ is the radial direction cosine. At emission and at each scattering event the frequency of the packet is recalculated according to the specified radial velocity field $v(r) \propto V_{\rm max}r^\alpha$ (see Section 3.3).

3.2   The geometry of the ejecta and the grid

The supernova ejecta is approximated by a three-dimensional Cartesian grid, each cell of which is assumed to have uniform density and composition. The grid is a cube with sides of width $2R_{\rm out}$ and a declarable number of divisions. After the initial emission of energy packets, the gas plays no further role in the simulation and thus only dust
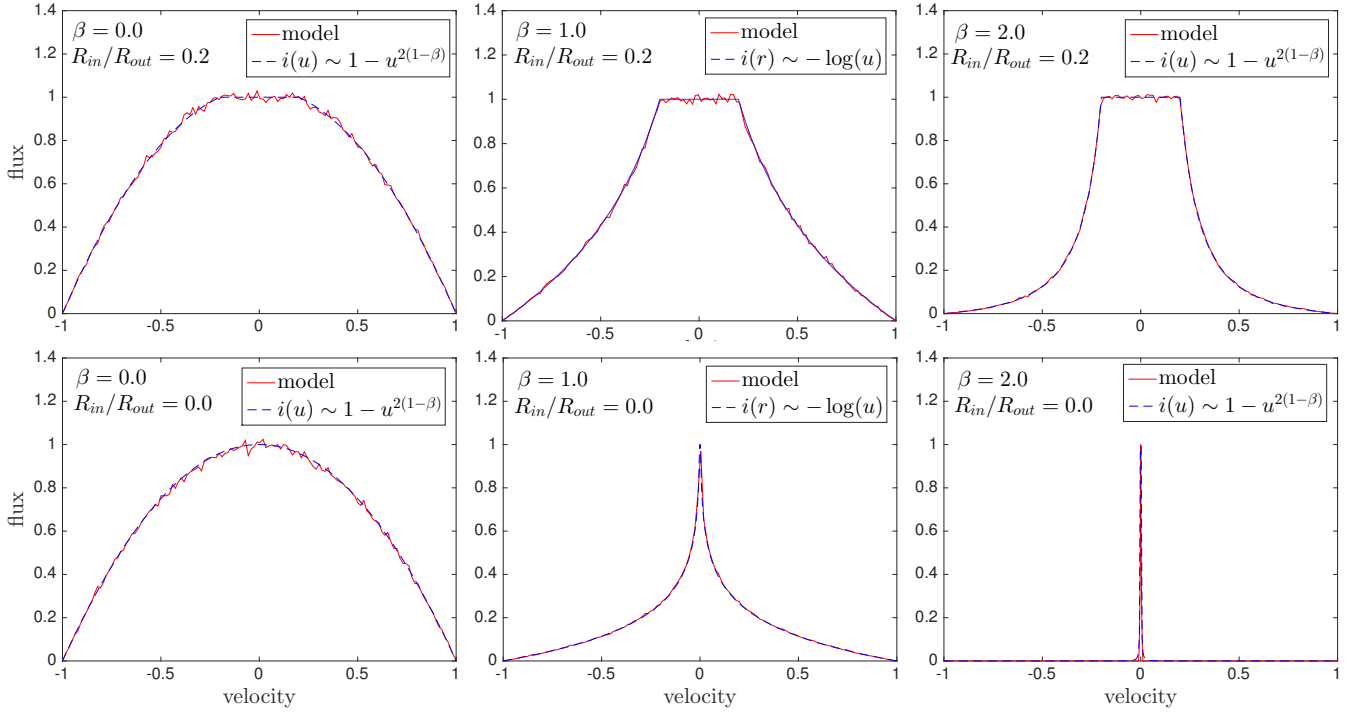
Figure 3. Red: benchmark models for optically thin ($\tau = 0$) line profiles with fractional velocity $v \propto r$. Left to right: initial emissivity profiles $i(r) \propto r^{-2\beta}$ with $\beta = 0.0, 1.0$ and 2.0. Cases with $R_{\rm in}/R_{\rm out} = 0.2$ are on the top and with $R_{\rm in}/R_{\rm out} = 0.0$ on the bottom. The presence of a plateau in the upper plots is due to the finite inner radius (detached shell). Blue: the analytical case with $i(u) \sim 1 - u^{2(1-\beta)}$ except in the case of $\beta = 1$ where $i(u) \sim -\log u$. Peak fluxes are scaled to unity.

properties are considered. By default, the dust is coupled to the gas (although it may be decoupled) and thus follows the smooth distribution described above ($\rho \propto r^{-\beta}$). The dust density in each cell is therefore calculated accordingly and any cell whose centre falls outside of the bounds of the supernova ejecta has density set to zero.

It is worth noting that if a constant mass-loss rate is required, the exponent of the velocity profile and the exponent of the density profile are not independent. A constant mass loss rate implies that $4\pi\rho v r^2 \propto k$, where k is a constant, and thus for $v \propto r^\alpha$ and $\rho \propto r^{-\beta}$, we require that $\beta - \alpha = 2$. However, it is possible that the supernova event may have induced a mass-flow rate that is not constant with radius and thus both exponents may be declared independently.

It is known from SED modelling that clumped environments produce very different results to environments assumed to have a smooth distribution of dust and gas. Specifically, clumped models tend to require a higher dust mass in order to reproduce a similar level of infrared dust emission compared to a smoothly distributed model. The capacity for modelling a clumped dusty medium is therefore included in the code. The fraction of the dust mass that is in clumps is declared ($m_{\rm frac}$) and the total volume filling factor of the clumps (f) is also specified. Dust that is not located in clumps is distributed according to a smooth radial profile. The clumps occupy a single grid cell and their size can therefore be varied by altering the number of divisions in the grid. The clumps are distributed stochastically with the probability of a given cell being a clump proportional to the

smooth density profile (i.e. $p(r) \propto r^{-\beta}$). The density within all clumps is constant and is calculated as

$$\rho_{\rm clump} = \frac{M_{\rm clumps}}{V_{\rm clumps}} = \frac{m_{\rm frac} M_{\rm tot}}{\frac{4}{3} f \pi (R_{\rm out}^3 - R_{\rm in}^3)} \qquad (4)$$

where $M_{\rm tot}$ is the total dust mass, $M_{\rm clumps}$ is the total dust mass in clumps and $V_{\rm clumps}$ is the total volume occupied by clumps. $m_{\rm frac}$ and f are defined as above.

3.3 The radiative transport mechanism

Following emission, a packet must be propagated through the grid until it escapes the outer bound of the ejecta at $R_{\rm out}$. The probability that the packet travels a distance l without interacting is $p(l) = {\rm e}^{-n\sigma l} = {\rm e}^{-\tau}$ where n is the grain number density, σ is the cross-section for interaction and $\tau = n\sigma l$ for constant n and σ (as in a grid cell). Noting that the probability that a packet will interact within a distance l is $1 - {\rm e}^{-\tau}$, we may sample from the cumulative probability distribution to give:

$$\xi = 1 - {\rm e}^{-\tau} \implies \tau = -\ln(1 - \xi) \qquad (5)$$

where $0 < \xi < 1$ is a random number sampled from a uniform distribution. The frequency of the photon packet and the mass density of the cell are then used to calculate the opacity of that cell. Using the fact that $n\sigma = \kappa\rho$, the distance l that the packet travels before its next interaction is calculated. If this value is greater than the distance from its position to the edge of the cell then the packet is moved

along its current trajectory to the cell boundary and the process is repeated. If the distance is less than the distance to the boundary then an event occurs and the packet is either scattered or absorbed, with the probability of scattering equal to the albedo of the cell

$$\omega = \frac{\sigma_{\mathrm{sca}}}{\sigma_{\mathrm{sca}} + \sigma_{\mathrm{abs}}} \qquad (6)$$

If the packet is absorbed then it is simply removed from the simulation as discussed above. If the packet is scattered then a new trajectory is sampled from an isotropic distribution in the comoving frame of the dust grain and the frequency of the packet is recalculated using Lorentz transforms subject to the velocity at the radius of the interaction (see Appendix A for further details). This process is repeated until the packet has either escaped the outer boundary of the supernova ejecta or has been absorbed. Escaped photon packets are added to frequency bins, weighted by w, in order to produce an overall emergent line profile. For our grain radii between 0.35μm and 3.5μm, Mie theory predicts grains to be forward scattering ($g = 0.7 - 0.8$). However, models that incorporate these values with the Henyey & Greenstein (1941) phase function are not significantly different to isotropically scattering grain models.

3.4 Properties of the Dusty Medium

Dust of any composition for which optical data are available may be used and the relative abundances of the species may be declared by the user. A grain size may be specified for each species. The extinction due to dust is only dependent on the cross-sectional area of the grains and not on the overall distribution. It is therefore not possible to determine details of a grain size distribution and only to constrain a single grain size parameter. The capacity to declare a size distribution is however included for the sake of ease of comparison with SED models. Mie theory and optical properties are used to calculate the overall $Q_{\mathrm{abs}}(\nu)$ and $Q_{\mathrm{sca}}(\nu)$ for each species and the derived opacities are summed over each species weighted according to their relative abundances.

As will be discussed in Section 4, the effects of scattering on the shapes of line profiles can potentially be quite pronounced and it is therefore important to consider the effects of electron scattering as well as those of dust scattering. Electron densities are estimated from the observed luminosity of Hα using an average temperature of 10,000 K and assuming that the electron density distribution is coupled to the emissivity distribution. The total optical depth to electron scattering between R_{in} and R_{out} is then calculated. Electron scattering is treated in an identical manner to dust scattering, with $\tau = \tau_{\mathrm{dust}} + \tau_{\mathrm{e}}$ in each cell. If, for a given packet, an event occurs, it is first calculated whether this is an electron scattering event or a dust event (either scattering or absorption) by considering the ratio of the optical depths to each. If the packet is scattered by an electron then the velocity of that electron is calculated by considering the bulk velocity at that radius and adding a thermal velocity component following the formalism described by Hillier (1991). The scattering process is then identical to that for dust. If the event is a dust event then the process continues

as described above. Including the electron scattering mechanism in models is optional.

In the majority of cases the electron scattering optical depths are not high enough to discernibly affect the overall shape of the profile. However, there may be some early epoch cases (the concept is discussed for SN 2010jl by Fransson et al. (2014)) where the electron scattering optical depths are high enough to have a significant effect on the observed profiles.

3.5 Technical details

DAMOCLES is written in FORTRAN 95 and parallelized for shared memory machines using OPENMP. It has been developed on and currently runs on a MacBook Pro 11.2 quad core with Intel Core i7 2.8GHz processors and 16GB of memory. A typical, medium resolution simulation using 125,000 grid cells and 10^5 packets takes approximately 15 s to run. The number of packets transported and the total dust optical depth are the most important factors in determining runtime. We intend to make DAMOCLES available in the public domain after some further development and documentation.

4 COMPARISON OF DAMOCLES MODELS WITH ANALYTICAL AND PREVIOUSLY PUBLISHED RESULTS

There is a general lack of published models in the literature that consider dust absorption-affected asymmetric line profiles. We therefore tested the code by comparing the results to optically thin profiles that may be derived analytically. We then tested the absorption and scattering components of the code by comparing our results for the case of an optically thick medium with those derived by Lucy et al. (1989) in their Model II and Model III scenarios.

4.1 Comparison of DAMOCLES models with analytical results

Analytical profiles may be calculated in the dust-free case. We ran a number of models based on the methods of Gerasimovic (1933) who derived equations for line profiles emitted from a transparent expanding shell.

Describing the fractional expansion velocity of the shell as $v(r) \propto r^\alpha$ with $\alpha \neq 0$ such that $v(r) = \frac{V(r)}{V_{\mathrm{max}}}$ where $V(r)$ and V_{max} represent physical velocities and $v_{\mathrm{max}} = 1$, the energy emitted by the nebula between line of sight velocities u and $u + du$ is proportional to

$$\int_\tau i(r) r \sin(\theta)\, r\, \mathrm{d}\theta\, \mathrm{d}r \qquad (7)$$

where $i(r)$ represents the emission per unit volume at radius r and θ is the angle to the observer's line of sight. We adopt inner radius $R_{\mathrm{in}} = q$ and outer radius $R_{\mathrm{out}} = 1$ such that $q = R_{\mathrm{in}}/R_{\mathrm{out}}$.

Setting $i(r) \propto r^{-2\beta}$ (for a recombination or collisionally

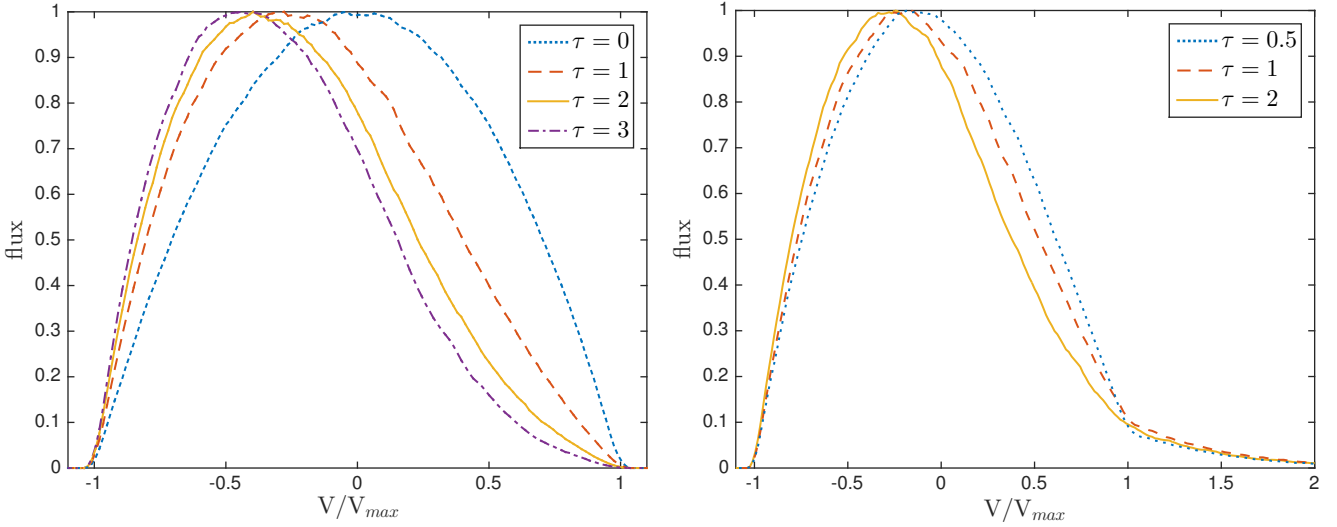**Figure 4.** Benchmark models for line profiles with $v \propto r$, $i(r) \propto$ constant and a filled sphere with $R_{in}/R_{out} = 0$. Pure dust absorption models ($\omega = 0$) are presented in the left-hand plots, whilst partially scattering models are presented on the right ($\omega = 0.6$) as per Lucy et al. (1989) Models II and III. All resulting profiles have been scaled to unit flux at their peaks.

excited line emitted from a medium with an assumed density profile for the emitter $\rho \propto r^{-\beta}$) then gives

$$
\begin{aligned}
i(u)\,\mathrm{d}u &\sim \frac{\mathrm{d}u}{\alpha u^{\frac{2\beta-3+\alpha}{\alpha}}} \int_{\theta_0}^{\theta_1} \cos^{\frac{2\beta-3}{\alpha}}\theta \sin\theta\,\mathrm{d}\theta \\
&\sim \frac{\mathrm{d}u}{u^{\frac{2\beta-3+\alpha}{\alpha}}} \left[\frac{\cos^{\frac{2\beta-3+\alpha}{\alpha}}\theta}{2\beta-3+\alpha} \right]_{\theta_0}^{\theta_1}
\end{aligned}
\tag{8}
$$

for $\frac{2\beta-3}{\alpha} \neq -1$ where $i(u)\,\mathrm{d}u$ is the energy emitted in a volume element and θ_0 and θ_1 are the bounds of this element. The case $\frac{2\beta-3}{\alpha} = -1$ results in a logarithmic relationship.

In the case of a "filled" nebula, i.e. one where the inner radius is vanishingly small in comparison to the outer radius, we obtain

$$
i(u)\,\mathrm{d}u \sim \pm \frac{\mathrm{d}u}{(2\beta-3+\alpha)u^{\frac{2\beta-1+\alpha}{\alpha}}} \left(1 - u^{\frac{2\beta-3+\alpha}{\alpha}}\right)
\tag{9}
$$

If the nebula is not "filled", that is to say, the inner radius is some fraction of the outer radius and the remnant is a detached shell, the above formula becomes valid only from some critical value $u' = q^{\alpha}$ to $u = 1$. For $u < u'$, we obtain

$$
i(u)\,\mathrm{d}u \sim \pm \frac{\mathrm{d}u}{(2\beta-3+\alpha)} \left(\frac{1}{q^{\alpha}} - 1\right)
\tag{10}
$$

and therefore the top of the line is flat while the sides are sloping.

Crucially, the width of the flat section is determined by $u' = q^{\alpha}$ or simply $u' = q$ in the case where $v \propto r$, whilst the shape of the profile outside of the flat top is described by equation 9.

Profiles with a variety of shapes may be derived from these formulae depending on the relative values of α and β. Here we consider three main families of curves:

(i) $i(u) \sim u^{-\gamma} - 1$ $(\alpha > 0, 2\beta - 3 + \alpha > 0)$

(ii) $i(u) \sim 1 - u^{\gamma}$ $(\alpha > 0, 2\beta - 3 + \alpha < 0)$

(iii) $i(u) \sim -\log u$ $(\alpha > 0, 2\beta - 3 + \alpha = 0)$

where γ is defined as $\gamma = |\frac{2\beta-3+\alpha}{\alpha}|$.

Models are presented for each of these cases, both for a filled nebula and for a shell structure with $R_{in}/R_{out} = 0.2$. A velocity profile $v \propto r$ appropriate for supernova ejecta in the free expansion phase is used throughout (Li & McCray 1992; Xu et al. 1992; McCray 1996; Baron et al. 2005). Values of $\beta = 0, 1$ and 2 are adopted. Fig. 3 illustrates the excellent agreement between the analytical case and the models. All fluxes are scaled to unity at the peak.

4.2 Comparison of DAMOCLES models with previously published results

In addition to the tests for optically thin lines described above, we also compared our outputs to those derived by Lucy et al. (1989) in order to assess the accuracy of the scattering and absorption aspects of the code. We consider two similar cases, equivalent to Models II and III of Lucy et al. (1989). In the first case, dust with zero albedo (pure absorption) is uniformly distributed throughout a filled nebula with a velocity profile $v \propto r$. In the second case, the same scenario is considered but in a medium of dust with albedo $\omega = 0.6$.

In the first case, the profile may once again be derived analytically from the basic geometry using the fact that radiation will be attenuated by a factor $e^{-2\tau_{\nu}v}$ between points with line-of-sight fractional velocities $-v$ and $+v$ where τ_{ν} is the optical depth at frequency ν from the centre to the outer edge of the ejecta. The line profile is therefore given by

$$
\frac{I(v)}{I(-v)} = \exp(-2\tau_{\nu}v)
\tag{11}
$$

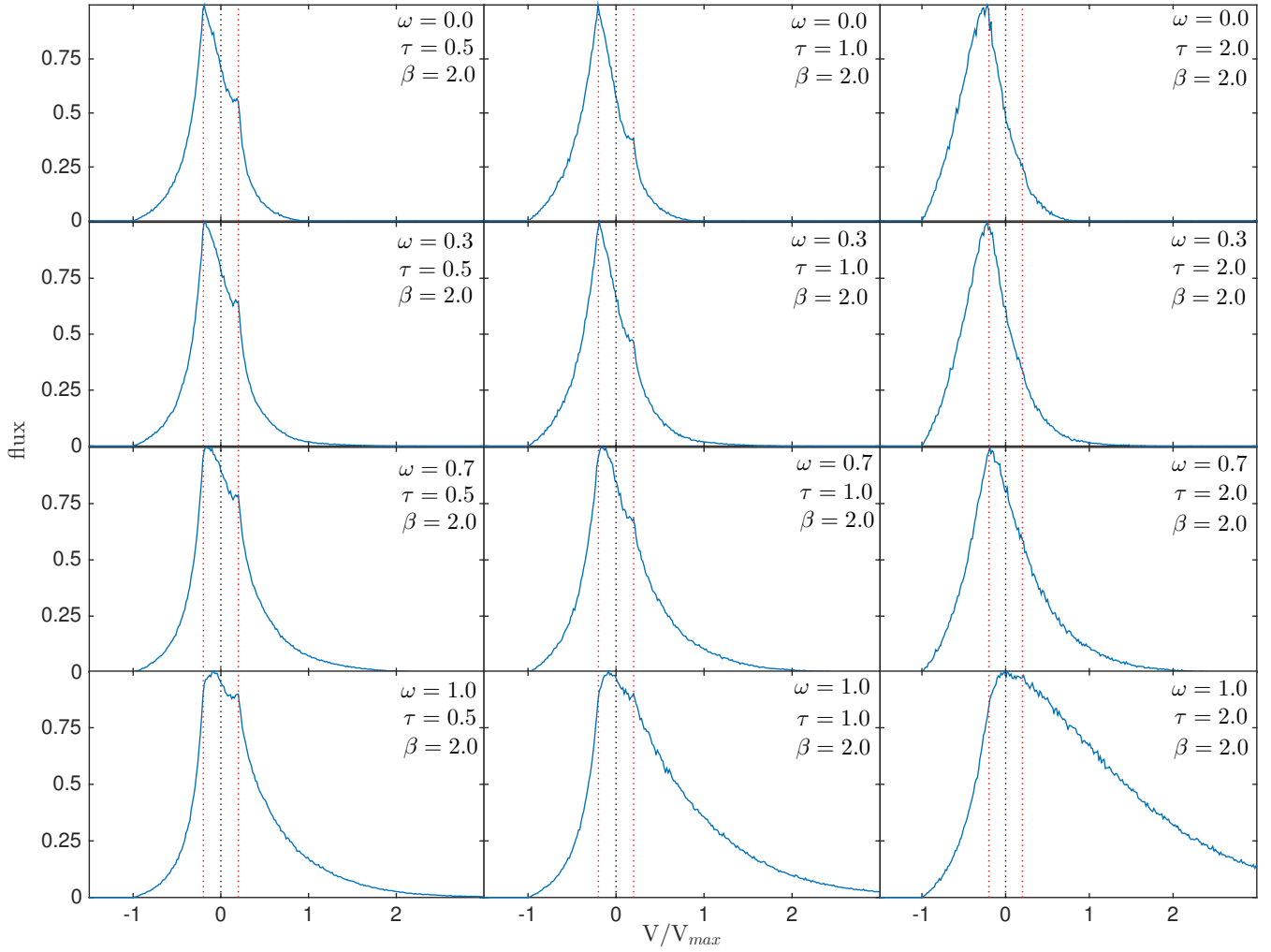Lucy et al. (1989) presented several examples for both

Figure 5. Set of models with $i(r) \propto r^{-4}$ (i.e. $\beta = 2.0$), $R_{\text{in}}/R_{\text{out}} = 0.2$, $v(r) \propto r$ and $v_{\text{max}} = 1$ illustrating the effects of varying the dust optical depth τ and albedo ω. Peak fluxes are scaled to unity. The black dotted line marks $v = 0$ and the red dotted lines mark $-v_{\text{min}}$ and $+v_{\text{min}}$.

the analytical case of the perfect absorber and a Monte Carlo model for grains with $\omega = 0.6$. We present the same cases in Fig. 4 and note that the resulting profiles exhibit the same features and shape. Of particular interest is the scattering wing that appears beyond the maximum velocity ($v_{\text{max}} = 1$) on the red side of profiles in the partial scatterer case as a result of the packets doing work on the expanding sphere. This was noted by Lucy et al. (1989) as a potential diagnostic for the presence of dust in the ejecta of a supernova and we will discuss this further in Section 4.3.

4.3 The sensitivity of the variable parameters

It is of general interest to establish potential diagnostic signatures in the line profiles of supernovae and their remnants in order to trace dust formation more effectively. We here discuss the effects of the main parameters of interest, namely:

- the maximum velocity V_{max}
- the ejecta radius ratio $R_{\text{in}}/R_{\text{out}}$

- the dust optical depth τ
- the dust albedo ω
- the density profile index β, where $\rho \propto r^{-\beta}$

4.3.1 The maximum velocity V_{max}

The maximum velocity is defined as the velocity at the outer edges of the line emitting region for a given line. The maximum velocity may vary between different spectral lines or doublets due to different locations of species having differing ionization thresholds. Clearly, the larger the maximum velocity used the wider the profile becomes. To some extent therefore the steepness of the density profile and the maximum velocity can act to counter each other since a steeper density distribution narrows the profile (see Section 4.3.5). The shape of the wings of the profiles, however, generally precludes much degeneracy in this aspect – the overall shape of the line profile can be used to determine the exponent of the density distribution to within a relatively small range.

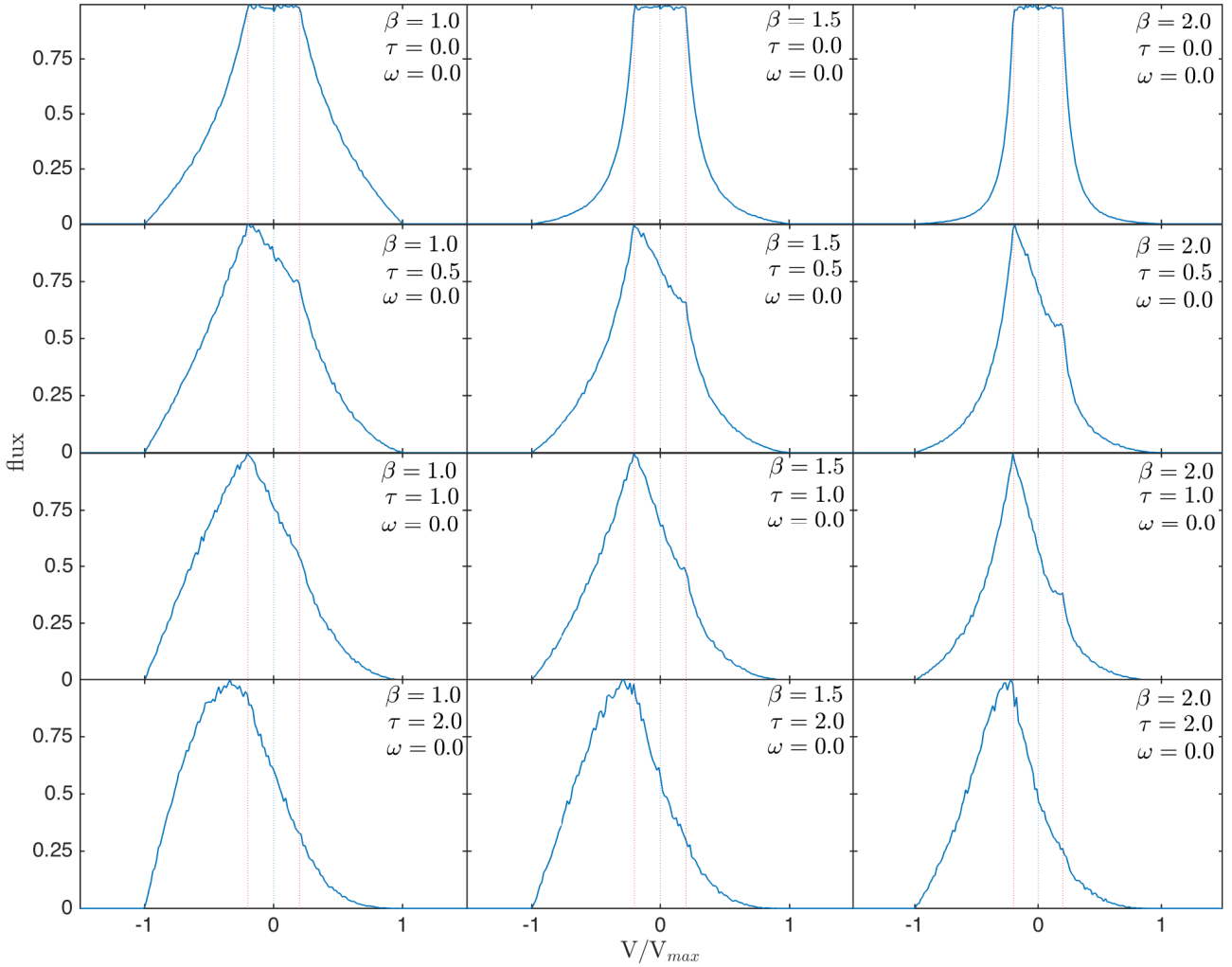More important is the effect that the maximum veloc-

Figure 6. Set of models with $i(r) \propto r^{-2\beta}$ for $\beta = 1.0$ *(left)*, $\beta = 1.5$ (middle) or $\beta = 2.0$ *(right)*, $\omega = 0$, $R_{\rm in}/R_{\rm out} = 0.2$, $v(r) \propto r$ and $v_{\rm max} = 1$ illustrating the effects of varying the dust optical depth τ. Peak fluxes are scaled to unity. The black dotted line marks $v = 0$ and the red dotted lines mark $-v_{\rm min}$ and $+v_{\rm min}$.

ity has on the overall optical depth. Since the outer radius is calculated directly from the maximum velocity (as $R_{\rm out} = V_{\rm max} \times t$ where $V_{\rm max}$ is determined from the blue side of the observed line profile), the overall volume of the ejecta is determined solely by this value and the ratio of the inner and outer radii. The total dust optical depth to which the radiation is exposed can therefore be greatly affected by even a relatively small change in the maximum velocity for fixed values of the other parameters. Practically, however, the maximum velocity can usually be fairly well determined from the observations (identified as the point where the flux vanishes on the blue side) and may be further constrained through modelling.

4.3.2 The ejecta radius ratio $R_{\rm in}/R_{\rm out}$

As already discussed in Section 4.1, the width of the flat top is determined by the ratio of the inner and outer radii, the exponent of the velocity profile and the maximum velocity. We assume that the supernova is in free expansion from

just a few months after the explosion and therefore $r = vt$ such that within the ejecta the velocity profile takes the form $v \propto r$ at a fixed time i.e. the supernova expands self-similarly (Li & McCray 1992; Xu et al. 1992; Kozma & Fransson 1998b). For this case, $R_{\rm in}/R_{\rm out}$ is given by

$$\frac{R_{\rm in}}{R_{\rm out}} = \frac{V_{\rm min}}{V_{\rm max}} \qquad (12)$$

where it is often possible to constrain $V_{\rm min}$ and $V_{\rm max}$ to a relatively narrow range simply from the observed line profile.

The majority of spectral lines emitted from supernovae and supernova remnants are expected to have a flat top before dust attenuation effects since it is rare for these objects to form a completely filled nebula. However, even a very small amount of dust attenuation may result in the line profile appearing to be smoothed at its peak.

The effects of absorption by dust on a line profile for a filled nebula with $R_{\rm in}/R_{\rm out} = 0$, as opposed to a detached shell, are shown in Fig. 4. All profiles have been scaled to unit flux at their peaks.
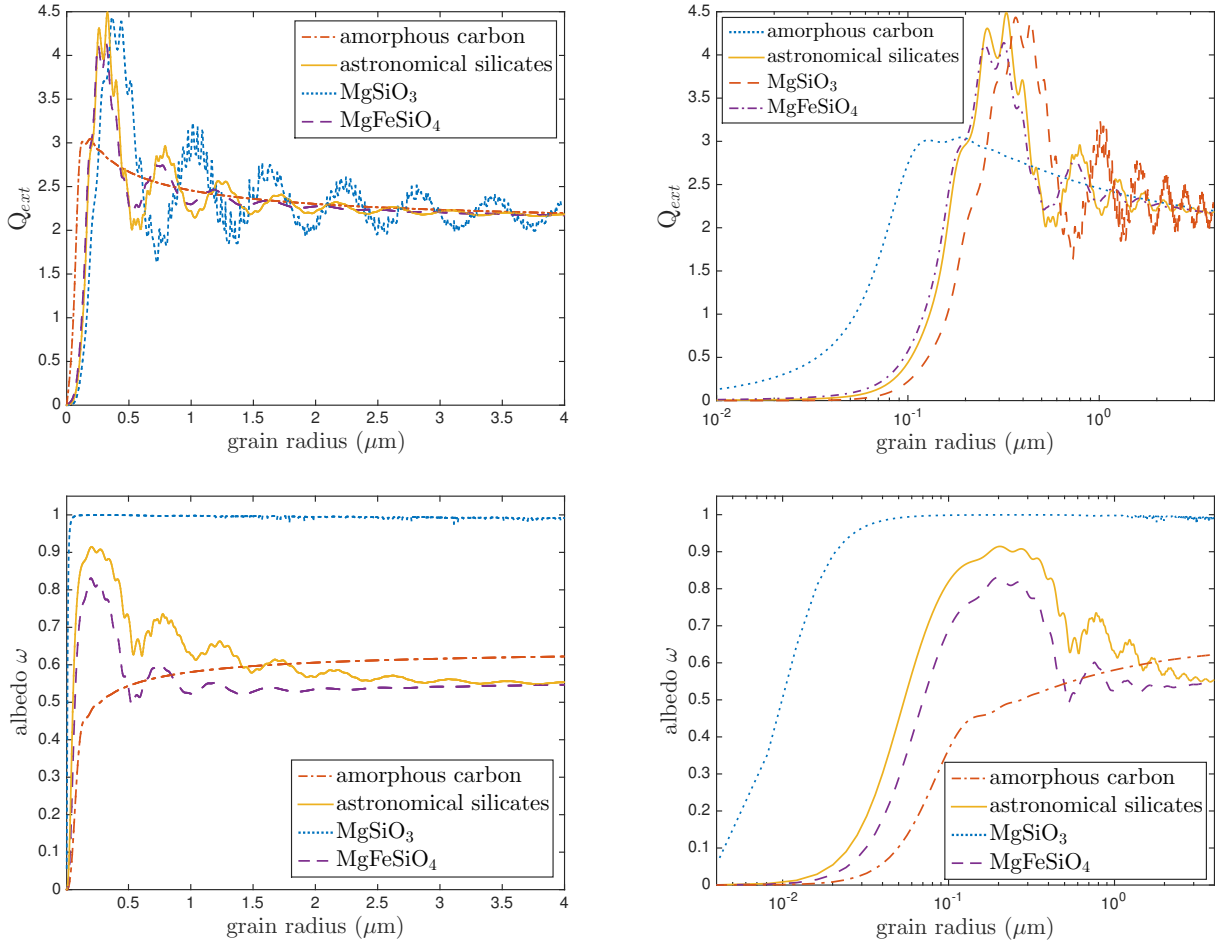
Figure 7. The variation of albedo and extinction efficiency (Q_{ext}) with grain radius at $\lambda = 656$ nm for Zubko et al. (1996) BE amorphous carbon, Draine & Lee (1984) astronomical silicate and the $MgSiO_3$ and $MgFeSiO_4$ samples of Jäger et al. (2003) and Dorschner et al. (1995), respectively. A linear grain size scale is presented on the left and a log scale on the right.

4.3.3   The dust optical depth τ (detached shell case)

As expected, greater attenuation of the original line profile is seen on the red side (see Figs 5 and 6). The profiles are most revealing at lower dust optical depths since the effects of the asymmetric absorption can be seen in different sections of the profiles and the profiles therefore tend to exhibit more features. The region of the profile that is most clearly affected by dust absorption is the flat-topped region. A small amount of absorption in this region results in a skewed profile, with a fraction of the flat-topped section removed. The peak becomes blueshifted as a result, but only to the original value of $-V_{min}$, the minimum velocity corresponding to R_{in}. In addition to the attenuation in this region, the red wing of the profile is also somewhat reduced, and the blue wing somewhat increased relative to their original symmetric positions. The result is a relatively "jagged" looking profile, often with sharp changes at $\pm V_{min}$. The profile is generally asymmetric, although the degree of absorption in the flat-topped region may sometimes make it seem as though the profile is in fact symmetric and uniformly blueshifted (see Section 4.5 for further discussion). Observationally, these sharp features might become smoothed due to insufficient spectral resolution.

At high dust optical depths or when the ratio of the inner and outer radii is small, the entire profile is shifted to the blue and the peak moves beyond $-V_{min}$ further into the blue. The profiles also tend to become more smooth and featureless. A set of models showing the effects of varying optical depths for different density profiles and dust albedos are presented in Figs 5 and 6 with $R_{in}/R_{out} = 0.2$.

4.3.4   The dust albedo ω

In the past, there has often been a focus on the effects of absorption by dust on the shapes of line profiles and less attention has been paid to the potential effects of scattering by dust. In fact, line profiles can be significantly affected by scattering of radiation. The greater attenuation of radiation received from the receding portion of the ejecta results in an asymmetry of the line profile whereby the majority of the observed emission is located bluewards of the peak. However, the effects of repeated dust scattering events within the ejecta can substantially alter the shape of a line profile and potentially can act to counter the blueshifted asymmetry.

Not only does repeated scattering of photons increase

the number of potential opportunities for a given photon to be absorbed but it also results in continuous shifting of the frequency of the photon to the red. The photon must do work on the expanding shell of dust in order to escape and thus many of the photons are reprocessed beyond the theoretical maximum velocity on the red side of the profile. Even in the case of dust grains with a relatively low albedo, a surprisingly persistent wing on the red side of the profile is seen, generally beyond the maximum theoretical velocity of the emitting region. In the case of strong dust scattering and high dust optical depths, this can actively result in a shift in the overall asymmetry of the profile, with the majority of the emission being emitted redwards of the peak. The peak however, remains blueshifted (for example the bottom left panel of Fig. 5) or central (for example the bottom right panel of Fig. 5). For the line profile to exhibit this effect requires the dust to be a nearly perfect scatterer; of the albedos plotted in Fig. 7 only the nearly transparent $MgSiO_3$ sample of Jäger et al. (2003) exhibits such a behaviour.

The combination of relatively low dust optical depths, initially flat-topped profiles, greater attenuation on the blue side along with increased flux on the red side due to scattering can result in a profile that sometimes ends up appearing almost symmetrical, particularly if contaminants, such as narrow lines or blending with other broad lines, are present or if the resolution of the data is low. The potential for apparently symmetrical profiles that appear to have been uniformly blueshifted should be noted (see Figs 5 and 6 for examples of this).

4.3.5 Density profile $\rho \propto r^{-\beta}$

Whilst the density profile of the dust may have some effect on the resulting profiles, it is the initial emissivity profile (dependent on the gas density profile) that has the greatest effect on the shape of the line profile. In general, the steeper the emissivity distribution, the narrower the line profile becomes. The sides of the line profile may become almost vertical for a very steep distribution since the majority of the emission then comes from a very narrow velocity range (see Figure 3).

The dependence of the shape of the line profile on the emissivity distribution is described analytically in Section 4.1 for the case of very optically thin dust. However, for even fairly low dust optical depths, the density profile plays a significant role in determining the shape of the line profile where it is affected by dust absorption. As previously discussed, at relatively small optical depths for reasonable R_{in}/R_{out}, a section of the flat-topped region is removed resulting in a peak at $-V_{min}$. The shape of the profile in this region is significantly affected by the density profile. Shallow density profiles (low β) produce a virtually linear variation in flux between $-V_{min}$ and $+V_{min}$ (for example the profiles in the left-hand column of Fig. 6). For a fixed dust optical depth, the steeper the distribution becomes, the more concave the profile becomes between $-V_{min}$ and $+V_{min}$, ultimately resulting in a clear shoulder to the profile at $+V_{min}$ (for example the profiles in the right-hand column of Fig. 6). For extremely steep density distributions this can result in a double peaked profile with a trough to the red of $V = 0$. An illustration of the effects on the line profiles of varying β and τ is shown in Fig. 6. As previously noted, these features may

not be apparent in observed line profiles with poor spectral resolution.

4.4 Inferring properties of the dust from the models

The presence of an extended red wing at large positive velocities in combination with increased extinction on the red side at smaller positive velocities can allow the values of τ and ω to be well constrained. Where this occurs it is possible to translate these values into a dust mass and grain size for a given species or combination of species using grain optical properties and Mie theory (see Figure 7).

For amorphous carbon, the albedo generally increases with grain size. The presence and extent of any scattering wing on the red side of the observed profile can therefore help to place limits on the grain radius. However, the greater the grain radius used the smaller the available cross-section for interaction per unit dust mass. Larger masses of dust are therefore required to fit the same degree of absorption if a larger grain size is used. This is in contrast to SED radiative transfer modelling where larger grain sizes generally result in less dust being required to fit the IR portion of the SED (W15). These two techniques in tandem may therefore provide limits on grain sizes for different species or combinations thereof.

It is known that the use of different optical properties may substantially alter dust masses derived using SED fitting for a given species of specific grain size (e.g. Owen & Barlow (2015)). However, the use of different sets of grain optical constants in our models seems to have only a minor effect on the required dust masses, except for cases where the albedo is close to unity (pure scattering grains).

4.5 The wavelength dependence of dust absorption

The greater the dust optical depth, the more attenuation of the line there will be. As expected, the red side of the profile suffers a greater degree of absorption than the blue side. The resulting asymmetry is somewhat more complex than perhaps previously thought. Dust has repeatedly been cited as the agent responsible for the apparent blueshifting of supernova line profiles in the manner of the profiles presented in Fig. 4; that is, relatively high optical depths result in an overall shift of the entire profile towards the blue. The relationship between the blueshifting of the peaks of profiles and their wavelength has been discussed by several authors in relation to dust formation (Smith et al. 2012; Fransson et al. 2014; Gall et al. 2014).

In practice, a relatively large dust optical depth is required to actively shift the peak of the profile bluewards of its natural $-V_{min}$ position (corresponding to the velocity at the inner radius of the shell) unless this value is very small in comparison to V_{max} i.e. the profile originally had a very narrow flat top. In many cases, it seems likely that the dust may not be optically thick and the blueshifting of the peak of the profile is just a result of attenuation in the flat-topped section (close to R_{in}). The peak would then tend to be located at $-V_{min}$.
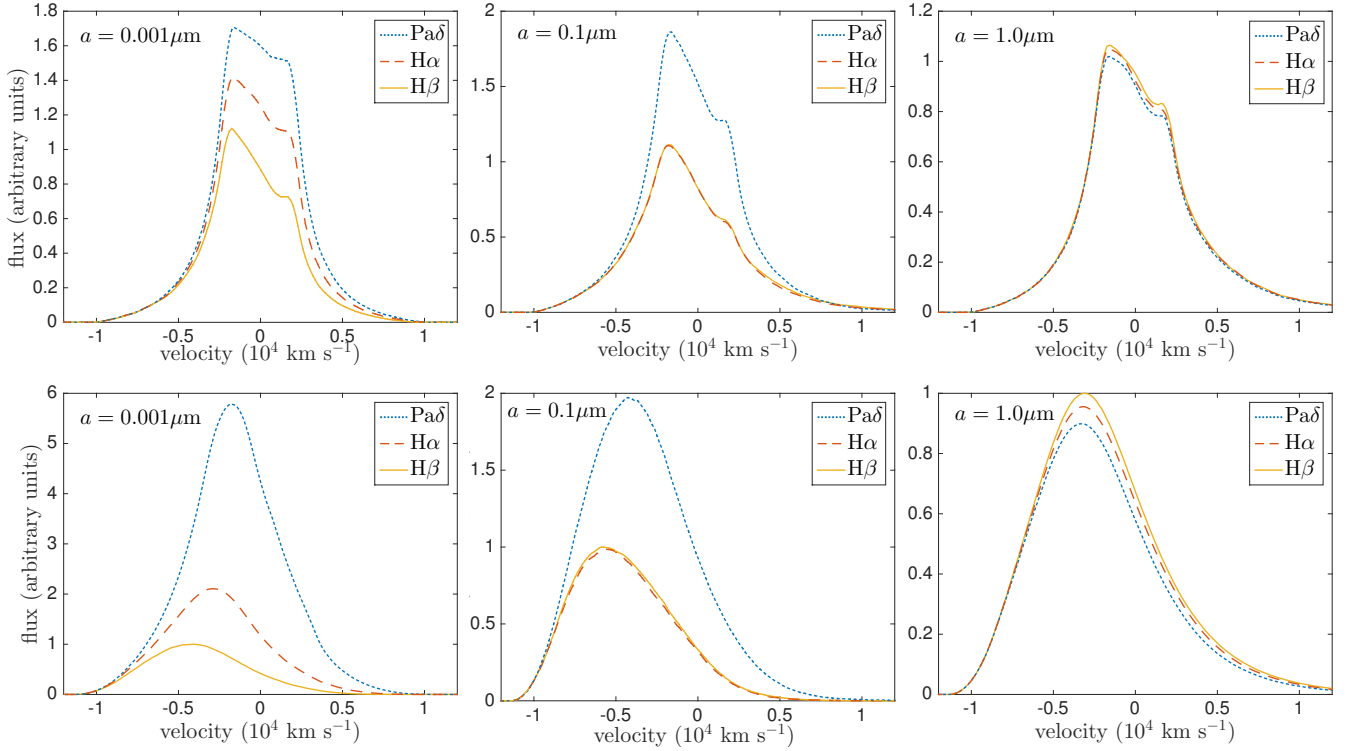
Since dust absorption is wavelength dependent for

Figure 8. Model line profiles for Hα (6563Å in *red*), Hβ (4861Å in *yellow*) and Paδ (10049Å in *blue*) for optically thin *(upper)* and optically thick *(lower)* cases respectively. All models adopted density profile $\rho(r) \propto r^{-4}$ (i.e. $\beta = 2$), velocity profiles $v(r) \propto r$ and radii ratio $R_{in}/R_{out} = 0.2$. The grain radii used were $a = 0.001$ μm *(left)*, $a = 0.1$ μm *(middle)* and $a = 1.0$ μm *(right)*. All the above models used Zubko et al. (1996) BE amorphous carbon.
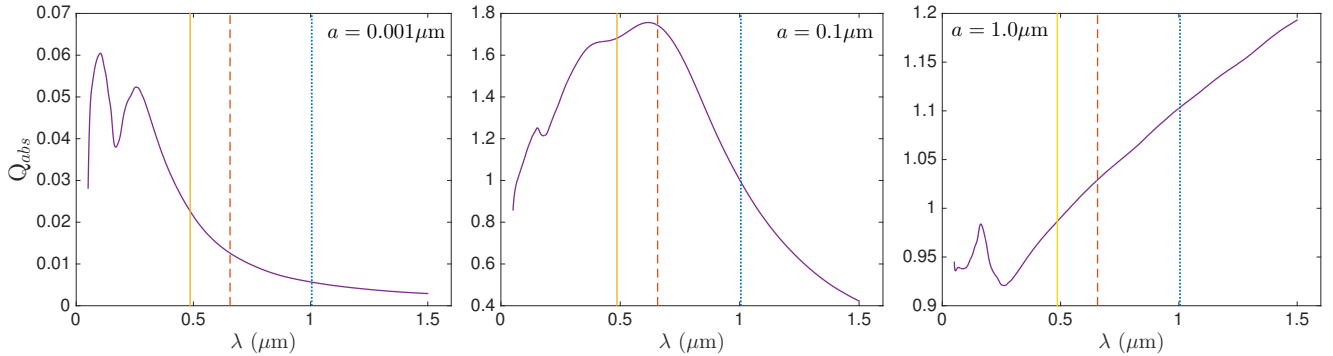

Figure 9. The variation of amorphous carbon dust absorption efficiency with grain size. The grain radii plotted are $a = 0.001$ μm *(left)*, $a = 0.1$ μm *(middle)* and $a = 1.0$ μm *(right)*. The vertical lines mark the wavelengths of Hα (6563Å in red), Hβ (4861Å in yellow) and Paδ (10049Å in blue).

$2\pi a < \lambda$, one might expect the position of the peak line flux to be dependent on the wavelength of the line being considered. We note here that whilst variations of the peak velocity of a line as a function of line wavelength may occur in cases of high dust optical depths or small R_{in}/R_{out}, this may not be the case for many supernova lines emitted from ejecta with low dust optical depths. The wavelength-dependence of dust absorption instead can result in differing degrees of extinction in the flat-topped region of each profile but still leave the peak at its blueshifted position of $-V_{min}$. If this is the case then there would be no reason to expect

a variation in the position of the peaks of profiles to be correlated with the wavelength dependence of dust absorption. Instead one would expect it potentially to trace the location of different ions within the ejecta, possibly with different V_{min} values observed for different species.

For lines from the same ion, for example the Balmer and Paschen lines of HI, we might expect to see peaks at the same position but differing degrees of absorption. At high spectral resolutions, it might be possible to detect differences in the shapes of the line profiles, particularly between $-V_{min}$ and $+V_{min}$ where the steepness of the incline traces the degree
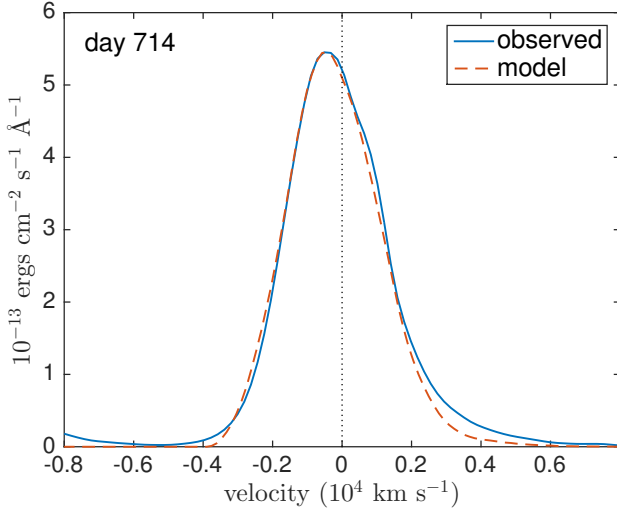
Figure 10. Amorphous carbon smooth dust fit to the day 714 Hα line of SN 1987A using an MRN size distribution, illustrating the underestimation of the red scattering wing for small grain radii. Model parameters are the same as the smooth dust fit for day 714 (Table 4) except for the grain size distribution and dust mass: $M_{\rm dust} = 8.0 \times 10^{-6} M_{\odot}$, $a_{\rm min} = 0.005\ \mu{\rm m}$, $a_{\rm max} = 0.25\ \mu{\rm m}$ and $n(a) \propto a^{-3.5}$.

of dust absorption. This can be seen in Figure 8 where we illustrate the effects of the wavelength dependence of dust absorption for three lines, Hα (6563Å), Hβ (4861Å) and Paδ (10049Å). All lines were modelled using three different grain sizes and for both optically thin and thick dust cases. We also show the variation of the absorption efficiency with wavelength for three different amorphous carbon grain sizes in Fig. 9.

5 RESULTS FOR SN 1987A

We have modelled the Hα line of SN 1987A at days 714, 806, 1862, 2211, 2875, 3500 and 3604, and the [O I] λ6300,6363 Å doublet at days 714, 806, 1054 and 1478. After day 3604 the Hα profile begins to become dominated by emission from the reverse shock and the structure of the emitting region may no longer be approximated by a single shell model as we do here (Fransson et al. 2013). The [O I] λλ6300,6363 Å doublet becomes too weak to model after day 1478 (see Fig. 1). We continue to adopt a velocity profile $V(r) = \frac{V_{\rm max}}{R_{\rm max}} r$ and treat the variable parameters listed at the start of Section 4.3. Whilst the albedo and optical depth are not varied directly, they are altered by adjusting the dust mass, $M_{\rm dust}$, and the grain size, a, which together determine the albedo and optical depth via Mie theory and the optical properties of the dust.

In all models, the ejecta occupies a shell with inner radius $R_{\rm in}$ and outer radius $R_{\rm out}$. Packets are emitted according to a smooth density profile assuming recombination or collisional excitation such that $i(r) \propto \rho(r)^2 \propto r^{-2\beta}$. Initially the dust is considered to have a smooth density distribution and is assumed to be coupled to the gas so as to follow the same radial profile. A clumped distribution of dust is considered later (see Section 5.2).

Table 3. Observed luminosities of the Hα line and estimated electron scattering optical depths from $R_{\rm in}$ to $R_{\rm out}$ for the radii detailed in Tables 4 and 5 based on an assumed gas temperature of 10,000 K.

day	Hα $L_{\rm obs}$ (10^{37} erg s^{-1})	$L_{\rm undep}/$ $L_{\rm obs}$	[O I] $L_{\rm obs}$ (10^{37} erg s^{-1})	$L_{\rm undep}/$ $L_{\rm obs}$	$\tau_{\rm e}$ (10^{-2})
714	1.36	1.65	0.313	3.57	1.44
806	0.57	1.77	0.0942	3.57	0.840
1054			0.0242	3.23	
1478			0.00185	2.70	
1862	0.0063	2.06			0.159
2211	0.0041	2.07			0.0378
2875	0.0019	2.84			0.0219
3500	0.00079	3.16			0.0125
3604	0.00098	3.27			0.0149

Assuming an electron temperature of 10,000 K, we estimated the total electron scattering optical depths between $R_{\rm in}$ and $R_{\rm out}$ based on the observed fluxes of the Hα recombination line. A temperature of 10,000 K for the recombining material is likely too high at the epochs considered but we adopt it in order not to underestimate electron scattering optical depths. The values we calculate from the observed Hα luminosities are listed in Table 3. Since the total electron scattering optical depths at these epochs are negligibly small we therefore do not include electron scattering in the models.

There is rarely a unique set of parameters that provide the best fit to the data. However, the majority of the parameters of interest can be well constrained from our modelling by considering different elements of the shape of the profile. In particular, by constructing fits to the data using minimum and maximum limits for the grain radius, credible lower and upper bounds on the dust mass formed within the ejecta may be derived. We present here fits to the data obtained using both small and large values of the grain radius a since it is the grain size which has the most significant effect on the overall dust mass required to reproduce the line profile (see Section 4).

All of our models are of a dusty medium composed solely of amorphous carbon grains. We use the optical constants from the BE sample presented by Zubko et al. (1996). Although previous SED modelling of SN 1987A limited the fraction of silicates present in the dusty ejecta to a maximum of 15% (Ercolano et al. (2007), W15), the recent work of Dwek & Arendt (2015) has suggested that a large mass of mostly silicate dust may have formed at early epochs (∼ 615 d). It is therefore useful to consider the effects on our models of using silicate dust. We discuss this in detail in Sections 5.7 and 5.8.

For each profile, the maximum velocity is initially identified from the data as the point where the emission vanishes on the blue side and is then varied throughout the modelling in order to produce the best fit. The equivalent point on the red side is indeterminate from observations due to the effects of dust scattering. We determine the approximate value of $V_{\rm min}$ by examining the width of the profile near its peak. Using the features and shapes presented in Figs 5 and 6 as a guide, we first examined the observed profile for any obvi-
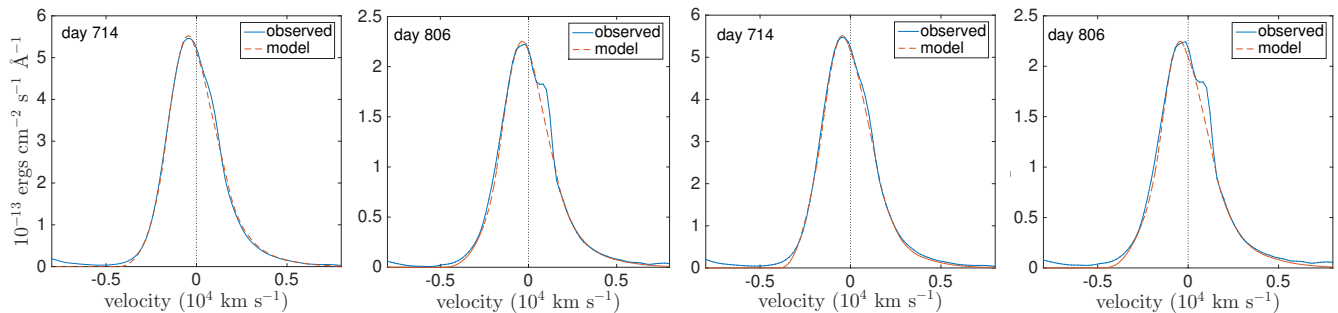
Figure 11. Best model fits to the SN 1987A Hα line at day 714 and day 806 for the parameters detailed in Tables 4 and 5. The two fits on the left are smooth dust models using amorphous carbon grains of radius $a = 0.35$ μm and the two fits on the right are clumped dust models using amorphous carbon grains of radius $a = 0.6$ μm.

ous points of inflection or abrupt changes in the steepness of the profile. If these were observed then they were compared to similar changes in theoretical profiles which allowed us to estimate the value of V_{min}. If none were observed, then a model setting V_{min} to be the velocity of the profile peak was considered. Where neither of these approaches yielded a good model (this was rare) we iterated over a range of values of V_{min} as with other variable parameters such as the dust mass. On the red side the theoretical minimum velocity often falls at a similar velocity to the 6583Å line so any dust-induced features near this wavelength that would allow a more accurate determination of V_{min} can be overwhelmed by the nebular line. Having determined the minimum and maximum velocities, the ratio of the inner and outer radii of the supernova ejecta can be determined since $R_{in}/R_{out} = V_{min}/V_{max}$. The outer radius is calculated from the epoch and the maximum velocity.

The only parameters that remain to be determined are the exponent of the density profile β, the mean grain radius and the total dust mass. The shape of the blue wing is solely a product of the density profile and the dust mass; the height and shape of the red wing is a product of these and also of the scattering efficiency of the grains (the albedo ω); the extent and shape of the asymmetry in the flat-topped portion of the profile is a function of only the total dust optical depth determined by the dust mass and the grain radius. By iterating over these three parameters, an excellent fit to the data can usually be obtained.

Models are produced in the same manner for the [O I] $\lambda\lambda6300,6363$ Å doublet as for the single Hα line, with each component of the doublet being modelled independently and the resulting profiles added according to a specified ratio. Although the theoretical intrinsic flux ratio is 3.1 for optically thin emission (Storey & Zeippen 2000), the actual ratio between the two components can be affected by self-absorption (Li & McCray 1992) and we therefore left it as a free parameter. The deduced doublet ratios are listed in Tables 4, 5 and 6.

For all lines, though particularly at very late epochs, even small fluctuations in the adopted value of the continuum level can have a substantial effect on the fit to the resulting profile. Since it is not feasible to establish the level of the continuum so precisely, the value of the continuum has been left as a free parameter that may be adjusted (to within sensible margins) in order to allow for the widest possible dust mass range to be determined. We generally find

it is necessary to assume a continuum level that is slightly lower where the dust mass is higher. The [O I]$\lambda6300,6363$ Å doublets at days 1054 and 1478 are weak relative to the continuum and are also blended with the wings of other lines making it difficult to fit their wings accurately. We aim to fit the lines between approximately -3000 km s^{-1} and $+5000$ km s^{-1} but present a wider velocity range for context (for example see Fig. 13).

Fits to the Hα line profile at days 2211 and 3500 are omitted for the sake of space but are very similar to those of days 1862 to 3604. All profiles have been smoothed to approximately the same resolution as the observed profiles using a moving-average procedure. Parameters for the models at all epochs including days 2211 and 3500 are detailed in Tables 4 to 6.

5.1 Smooth Density Models for SN 1987A

Even at the earliest epochs there is a substantial wing on the red side of the Hα line profile that cannot be fitted by scattering from moving grains with a low albedo. The minimum required albedo is approximately $\omega \approx 0.5$ implying relatively large grain radii. As previously discussed, the larger the grain size the larger the mass of dust required to reproduce the same optical depth. Fig. 10 illustrates the fit for the day 714 Hα profile for the case where a classic MRN (Mathis et al. 1977) grain size distribution is adopted, with $a_{min} = 0.005$μm, $a_{max} = 0.25$ μm and $n(a) \propto a^{-3.5}$. It can be seen clearly that the extended red wing is significantly underestimated. Since the albedo of amorphous carbon grains varies significantly with grain radius (see Fig. 7) we can establish a strong lower bound to the mean dust grain radius, which we estimate to be $a \geq 0.35$ μm. This is the smallest grain size that is still capable of reproducing the red scattering wing at all epochs and we therefore use this lower limit value throughout our smooth density modelling.

The inner and outer radii of the ejecta are calculated at each epoch from the maximum velocity used, the day number and the specified ratio R_{in}/R_{out}. The radii generated are consistent with those used in previous models of SN 1987A (Ercolano et al. (2007), W15) and the minimum velocities for both the [O I] and Hα line emitting regions are relatively consistent with those obtained by Kozma & Fransson (1998b) who estimate that hydrogen extends into the core to a depth of $\lesssim 700$ km s^{-1} and the oxygen reaches down to ~ 400 km s^{-1}. They are also consistent with predictions
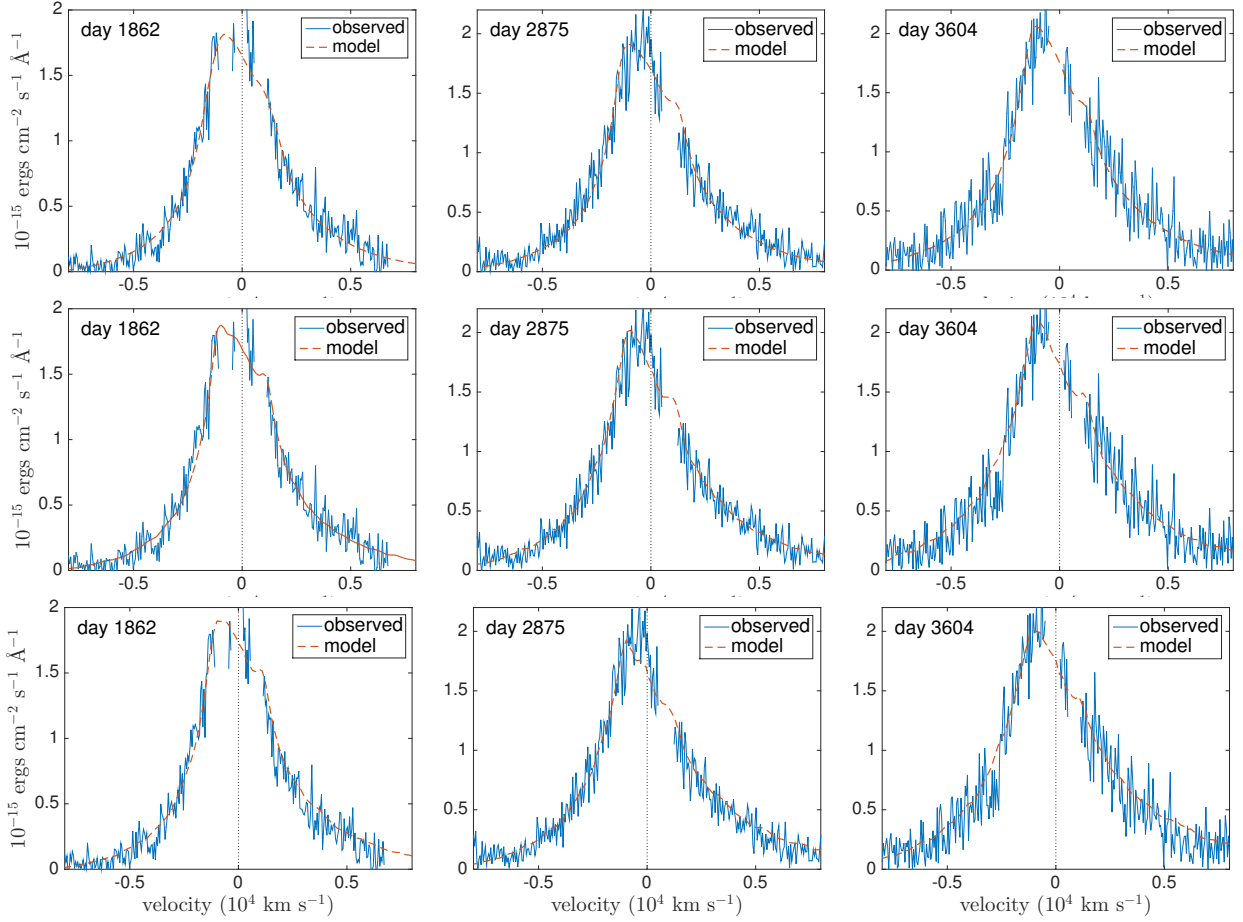
Figure 12. Best model fits to the SN 1987A Hα line at days 1862, 2875 and 3604 for the parameters detailed in Tables 4 – 6. On the top row are smooth model fits with amorphous carbon grains of radius $a = 0.35$ μm. On the middle and bottom rows are clumped model fits with amorphous carbon grains of radii $a = 0.6$ μm and $a = 3.5$ μm, respectively.

from 3D explosion models at the time of shock-breakout that predict the oxygen to reach to a depth of ~ 200 km s^{-1} (Hammer et al. 2010; Wongwathanarat et al. 2015). Figs 11 to 13 show the best fits to the data for days 714 to 3604 whilst Table 4 details the parameters used.

It can be seen from Tables 4 – 6 that, in order to reproduce the blueshifts seen in the [O I] λλ6300,6363 Å doublet, considerably larger dust masses are required than to fit the Hα line at the same epoch. Although the same maximum velocities and therefore outer radii are used in our [O I] and Hα models, the inner radii for the [O I] models are significantly smaller and the density distribution much steeper. This implies that [O I] is concentrated towards the centre of the ejecta whereas Hα is more diffuse. This is broadly in agreement with 3D explosion dynamics models that suggest that a few hours after the explosion the heavier elements will, in comparison to hydrogen, be located more centrally in the ejecta with "bullets" of heavier material reaching the outer edges (Hammer et al. 2010). If dust is forming in the inner regions of the ejecta then the majority of the [O I] emission must travel through the newly formed dust whereas the more diffuse Hα emission has a greater chance of escaping unaffected. This may explain the difference between the dust masses needed for the [O I] and Hα models.

5.2 Clumped Dust Models for SN 1987A

A number of investigators have presented arguments for the material in the ejecta of SN 1987A being clumped (Lucy et al. 1991; Li & McCray 1992; Kozma & Fransson 1998b) and so we consider clumped models for the ejecta dust to be more realistic than smoothly distributed dust models. It has been shown through the modelling of optical-IR SEDs that when dust is assumed to have a clumped distribution then the derived dust masses can be significantly larger than for the case of dust that is distributed smoothly between the inner and outer radii (e.g. Ercolano et al. (2007); Owen & Barlow (2015)). We present two sets of fits to the line profile based on the clumped dust modelling of W15, one set with a minimum grain size and one set with a maximum grain size. Each fit is based on the best fitting smooth model such that the photon packets are emitted assuming a smooth radial density profile. However, the dust is no longer coupled to the gas but instead is located entirely in clumps of size $R_{\rm out}/25$. The clumps are distributed stochastically between $R_{\rm in}$ and $R_{\rm out}$ with the probability of a given grid cell being a clump proportional to $r^{-\beta}$ where $i(r) \propto r^{-2\beta}$. The number of clumps used is determined by the clump filling factor f which is kept constant at $f = 0.1$. All properties are fixed

Table 4. The parameters used for the best fitting smooth models of SN 1987A with amorphous carbon grains of radius $a = 0.35$ μm. Optical depths are given from $R_{\rm in}$ to $R_{\rm out}$ at $\lambda = 6563$ Å for Hα and $\lambda = 6300$ Å for [O I]. Values of τ_V are very close to the quoted values of $\tau_{H\alpha}$.

	day	$V_{\rm max}$ (km s^{-1})	$V_{\rm min}$ (km s^{-1})	$R_{\rm in}/R_{\rm out}$	β	$M_{\rm dust}$ ($M_\odot$)	$R_{\rm out}$ (cm)	$R_{\rm in}$ (cm)	[O I] ratio	τ_λ
[O I]	714	3250	228	0.07	2.9	9.65×10^{-5}	2.00×10^{16}	1.40×10^{15}	2.6	3.60
[O I]	806	4000	240	0.06	2.4	1.50×10^{-4}	2.79×10^{16}	1.67×10^{15}	2.3	2.86
[O I]	1054	4300	215	0.05	2.1	2.35×10^{-4}	3.92×10^{16}	1.96×10^{15}	2.7	2.23
[O I]	1478	4500	180	0.04	1.7	2.95×10^{-4}	5.75×10^{16}	2.30×10^{15}	3.0	1.30
Hα	714	3250	813	0.25	1.2	2.10×10^{-5}	2.00×10^{16}	5.01×10^{15}		0.61
Hα	806	4000	880	0.22	1.9	3.80×10^{-5}	2.79×10^{16}	6.13×10^{15}		0.59
Hα	1862	8500	1275	0.15	1.9	5.00×10^{-4}	1.37×10^{17}	2.05×10^{16}		0.35
Hα	2211	9000	1260	0.14	1.9	9.25×10^{-4}	1.72×10^{17}	2.41×10^{16}		0.42
Hα	2875	9500	1330	0.14	1.9	1.50×10^{-3}	2.36×10^{17}	3.30×10^{16}		0.36
Hα	3500	10000	1400	0.14	1.9	3.35×10^{-3}	3.02×10^{17}	4.23×10^{16}		0.49
Hα	3604	10250	1333	0.13	1.9	4.20×10^{-3}	3.19×10^{17}	4.15×10^{16}		0.55

Table 5. The parameters used for the best fitting clumped models of SN 1987A with amorphous carbon grains of radius $a = 0.6$ μm. Optical depths are given from $R_{\rm in}$ to $R_{\rm out}$ at $\lambda = 6563$ Å for Hα and $\lambda = 6300$ Å for [O I]. Values of τ_V are very close to the quoted values of $\tau_{H\alpha}$.

	day	$V_{\rm max}$ (km s^{-1})	$V_{\rm min}$ (km s^{-1})	$R_{\rm in}/R_{\rm out}$	β	$M_{\rm dust}$ ($M_\odot$)	$R_{\rm out}$ (cm)	$R_{\rm in}$ (cm)	[O I] ratio	τ_λ
[O I]	714	3250	228	0.07	2.7	2.00×10^{-4}	2.00×10^{16}	1.40×10^{15}	2.3	3.84
[O I]	806	4000	240	0.06	2.3	4.00×10^{-4}	2.79×10^{16}	1.67×10^{15}	2.0	4.02
[O I]	1054	4300	215	0.05	2.3	7.50×10^{-4}	3.92×10^{16}	1.96×10^{15}	2.3	3.85
[O I]	1478	4500	180	0.04	2.0	1.10×10^{-3}	5.75×10^{16}	2.30×10^{15}	2.8	2.65
Hα	714	3250	813	0.25	1.4	5.50×10^{-5}	2.00×10^{16}	5.01×10^{15}		0.87
Hα	806	4000	880	0.22	1.8	9.00×10^{-5}	2.79×10^{16}	6.13×10^{15}		0.76
Hα	1862	8500	1190	0.14	1.9	1.20×10^{-3}	1.37×10^{17}	1.91×10^{16}		0.46
Hα	2211	9000	1260	0.14	1.9	3.00×10^{-3}	1.72×10^{17}	2.41×10^{16}		0.73
Hα	2875	9500	1140	0.12	2	8.00×10^{-3}	2.36×10^{17}	2.83×10^{16}		1.05
Hα	3500	10000	1200	0.12	2	1.35×10^{-2}	3.02×10^{17}	3.63×10^{16}		1.08
Hα	3604	10250	1230	0.12	2	1.70×10^{-2}	3.19×10^{17}	3.83×10^{16}		1.22

Table 6. The parameters used for the best fitting clumped models of SN 1987A with amorphous carbon grains of radius $a = 3.5$ μm. Optical depths are given from $R_{\rm in}$ to $R_{\rm out}$ at $\lambda = 6563$ Å for Hα and $\lambda = 6300$ Å for [O I]. Values of τ_V are very close to the quoted values of $\tau_{H\alpha}$.

	day	$V_{\rm max}$ (km s^{-1})	$V_{\rm min}$ (km s^{-1})	$R_{\rm in}/R_{\rm out}$	β	$M_{\rm dust}$ ($M_\odot$)	$R_{\rm out}$ (cm)	$R_{\rm in}$ (cm)	[O I] ratio	τ_λ
[O I]	714	3250	228	0.07	2.9	1.50×10^{-3}	2.00×10^{16}	1.40×10^{15}	2.3	4.20
[O I]	806	4000	240	0.06	2.3	2.70×10^{-3}	2.79×10^{16}	1.67×10^{15}	2.1	3.95
[O I]	1054	4300	215	0.05	2.3	5.50×10^{-3}	3.92×10^{16}	1.96×10^{15}	2.5	4.12
[O I]	1478	4500	180	0.04	1.9	8.00×10^{-3}	5.75×10^{16}	2.30×10^{15}	2.8	2.81
Hα	1862	8500	1190	0.14	1.9	1.00×10^{-2}	1.37×10^{17}	1.91×10^{16}		0.55
Hα	2211	9000	1260	0.14	1.9	2.40×10^{-2}	1.72×10^{17}	2.41×10^{16}		0.85
Hα	2875	9500	1140	0.12	2	6.00×10^{-2}	2.36×10^{17}	2.83×10^{16}		1.15
Hα	3500	10000	1200	0.12	2	1.15×10^{-1}	3.02×10^{17}	3.63×10^{16}		1.34
Hα	3604	10250	1230	0.12	2	1.25×10^{-1}	3.19×10^{17}	3.83×10^{16}		1.31

from the smooth models with the exception of the grain radius, density profile exponent (β) and the total dust mass.

Models were again constructed using the smallest possible grain radius (a=0.6 μm in the clumped case) in order to derive minimum dust masses for clumped distributions. By considering the extent of the red scattering wing, upper limits to the grain size were also derived with the purpose of limiting the maximum dust mass at each epoch. By steadily

reducing the grain radius from an initial value of 5 μm (motivated by the maximum possible grain size derived by W15 for their day 8515 model), we produced a set of models with a maximum grain radius of $a = 3.5$ μm.

The increase in grain size from the smooth case to the clumped case is necessary in order to have a slightly larger albedo. Grains of radius $a = 0.35$ μm do not reproduce the red side of the profiles well for a clumped medium. This is

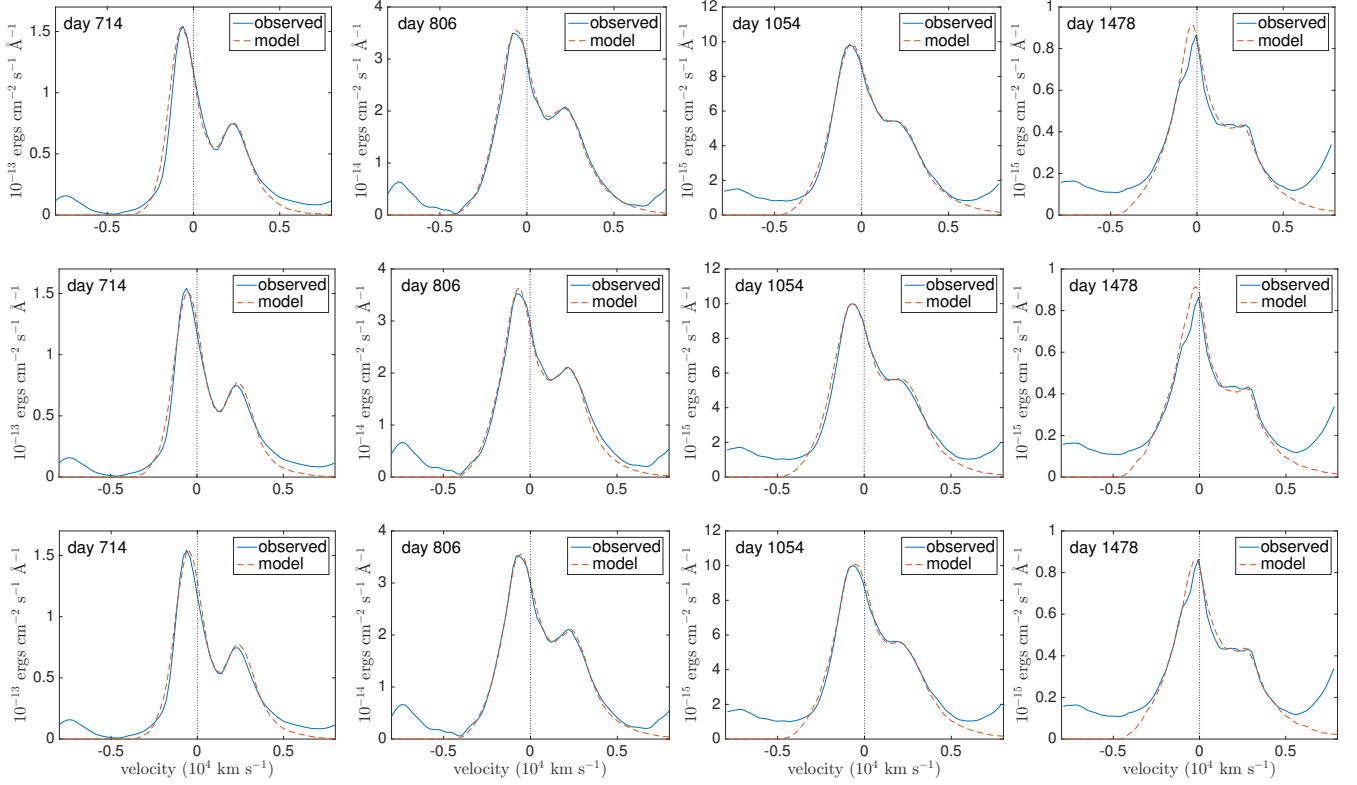**Figure 13.** Best model fits to the SN 1987A [O I] λ6300,6363 Å doublet at days 714, 806, 1054 and 1478 for the parameters detailed in Tables 4 – 6. On the top row are smooth dust fits with amorphous carbon grains of radius $a = 0.35\mu m$. On the middle and bottom rows are clumped dust fits with amorphous carbon grains of radii $a = 0.6\mu m$ and $a = 3.5\mu m$ respectively.

because when the dust is located in clumps the radiation is subject to less scattering as well as to less absorption. The reduction in scattering appears not to be compensated for by the increased dust mass and a larger grain radius is therefore required, particularly at day 714.

For all but the Hα line at days 714 and 806 a similar fit could be obtained with either a grain radius of $a = 0.6$ μm or $a = 3.5$ μm (see Figs 11 – 13). However, for Hα at days 714 and 806 even a small change to the grain radius from 0.6 μm resulted in a significantly poorer fit, either over-estimating or under-estimating the red wing. We therefore conclude that the dust mass estimates produced for the Hα lines at days 714 and 806 for a grain radius of $a = 0.6$ μm are the best Hα-based estimates of the dust mass at this epoch.

In our subsequent analyses, we adopt the values derived from our clumped models. Details of the parameters used are presented in Tables 5 and 6 and the fits are presented in Figures 11 and 12.

5.3 Goodness of fit

We detailed at the start of Section 5 the process by which parameters were constrained in order to obtain good fits to the data. These fits were judged both by eye and by minimizing the MSE between the model and the observed data for each line profile. For those interested in the sensitivity of the fits to various parameters, in Tables 7 and 8 we detail the mean

square error (MSE) for the Hα profile at days 714 and 2875 for a range of dust masses and density profile exponents. All other parameters were kept fixed at their best-fitting values for the clumped models of Hα with a grain radius $a = 0.6\mu m$ as in Table 5. The MSE is calculated as

$$\frac{1}{N}\sum_i (f_{\text{obs},i} - f_{\text{mod},i})^2 \qquad (13)$$

where N is the number of data points, $f_{\text{obs},i}$ is the observed flux at the ith data point and $f_{\text{mod},i}$ is the modelled flux at the ith data point. The MSEs were calculated between -5000 and $+7000$ km s^{-1} for the day 714 Hα profile and between -8000 and $+8000$ km s^{-1} for the day 2875 Hα profile. Note that the MSEs should only be compared between models for a given observed line profile and not between different line profiles since each observation is associated with a different inherent error.

For day 714, we find that increasing or decreasing the total dust mass by a factor of two with all other parameters fixed causes a substantial increase in the mean square error (by factors of 23 and 8.6 respectively) effectively ruling out these values. For day 2875 a similar variation is seen but with the MSE varying by factors of 1.4 and 3.0 for each case. The narrower range of MSEs at day 2875 compared to day 714 is due to a noisier profile which results in a greater allowed range of good fits. The sensitivity of the goodness of fit to the dust mass and density profile is similar for the other modelled epochs.

Table 7. MSEs illustrating the variation in goodness of fit for the Hα line profile for a range of dust masses with other parameters fixed at their best-fitting values for the clumped model with $a = 0.6\mu$m as detailed in Table 5. The MSE is calculated between -5000 and $+7000$ km s^{-1} for the day 714 Hα profile and between -8000 and $+8000$ km s^{-1} for the day 2875 Hα profile. A factor of zero represents the dust-free model. The best-fitting model is italicized.

| | multiple of best-fitting mass | | | | | |
	0	0.1	0.5	*1.0*	2.0	10
Day 714 MSE (10^{-13} erg cm^{-2} s^{-1})	0.167	0.133	0.043	*0.005*	0.115	1.15
Day 2875 MSE (10^{-15} erg cm^{-2} s^{-1})	0.0791	0.0604	0.0258	*0.0182*	0.0563	0.288

Table 8. Mean square errors illustrating the variation in goodness of fit for the Hα line profile for a range of density profiles with other parameters fixed at their best-fitting values for the clumped model with $a = 0.6\mu$m as detailed in Table 5. The MSE is calculated between -5000 km s^{-1} and $+7000$ km s^{-1} for the day 714 Hα profile and between -8000 km s^{-1} and $+8000$ km s^{-1} for the day 2875 Hα profile. The best-fitting model is italicised.

| | density profile exponent (β) | | | | |
	1.0	1.2	*1.4*	1.6	1.8
Day 714 MSE (10^{-13} erg cm^{-2} s^{-1})	0.0328	0.0117	*0.005*	0.0184	0.0410
	1.6	1.8	*2.0*	2.2	2.4
Day 2875 MSE (10^{-15} erg cm^{-2} s^{-1})	0.0282	0.0205	*0.0182*	0.0193	0.0255

5.4 The effects of clumping

As in the case of SED radiative transfer models, the dust masses required to reproduce the observations in the clumped scenario are considerably higher than for the smooth scenario. The dust masses differ between our smooth models for $a = 0.35\ \mu$m and clumped models for $a = 0.6\mu$m by a factor of approximately 3. The dust mass estimates are even larger when comparing clumped $a = 0.6\ \mu$m models to clumped $a = 3.5\ \mu$m models at later epochs. This does not take into account the increase in grain radius between the two cases however. This increase accounts for a reasonable fraction of this difference. We estimate the effects of clumping alone to increase the required dust mass by a factor of approximately 1.5-2.0 from the smooth case.

5.5 More complex models

Where blueshifted lines are observed in the spectra of CCSNe it is often the case that the Balmer lines of HI are less affected than the [O I] lines (Milisavljevic et al. 2012). This may be due to a difference in the location or distribution of the emitting elements; if the neutral hydrogen was diffusely distributed throughout the envelope but the oxygen was co-located with the dust in the core and in clumps then this could result in [O I] emission undergoing greater attenuation than Hα. This geometry would be in line with previous models of SN 1987A that suggested that the dust-forming regions are likely to include those which are oxygen-rich (Kozma & Fransson 1998a). Clearly, any model of dust formation in the ejecta of a CCSN must consistently reproduce all of the line profiles at a given epoch. The models presented in this paper thus far have coupled the gas and dust distributions for a fixed clump volume filling factor and clump size. The Hα and [O I] models therefore require dif-

ferent dust masses with the [O I] models usually requiring a dust mass ~ 4 times larger than the Hα models.

We now present a model that reconciles this difference by additionally varying the clump filling factor, clump size and emissivity distribution. We assume that neutral hydrogen is likely diffuse throughout the ejecta and so maintains a smoothly distributed power-law emissivity distribution between $R_{\rm in}$ and $R_{\rm out}$ for Hα. However, we now assume that dust mostly forms in dense regions of high metallicity and so restrict the [O I]λ6300,6363 Å emission to originate largely from the dusty clumps with only a small fraction emitted from the inter-clump medium. As previously discussed, the greater the covering factor of the dust the greater the albedo required in order to reproduce the Hα red scattering wing. In order to obtain both the strong blueshifting of the [O I] line and the extended red scattering wing observed in Hα a small number of dense clumps were required along with a small mass of diffusely distributed highly scattering dust in the inter-clump medium.

In order to fit both line profiles simultaneously, we required a very high albedo ($\omega > 0.8$) that demanded the inclusion of some fraction of silicate dust. Amorphous carbon grains alone are incapable of producing this level of scattering for any grain size. We adopted a grain radius of $a = 0.6\mu$m, the same as that used in our initial clumped models and we varied the relative proportions of amorphous carbon and MgSiO$_3$ in order to achieve the necessary albedo. The adopted grain densities were $\rho_{\rm c} = 1.85$ g cm^{-3} for amorphous carbon grains and $\rho_{\rm s} = 2.71$ g cm^{-3} for MgSiO$_3$. The resulting dust model for day 714 used 75% MgSiO$_3$ and 25% amorphous carbon by cross-sectional area with a volume filling factor $f_V = 0.1$ and a clump size $R_{\rm out}/5$. 90% of the dust mass was located in clumps with the remaining 10% distributed smoothly between $R_{\rm in}$ and $R_{\rm out}$ according
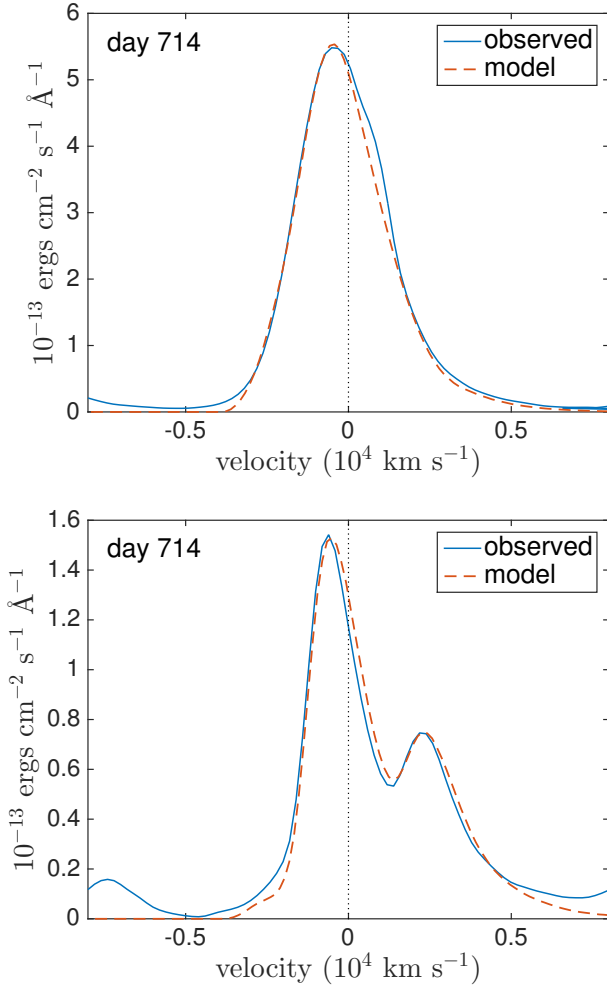
Figure 14. Fits to the Hα and [O I]λ6300,6363 Å lines at day 714 using the more complex dust model described in Section 5.5 with a dust mass of $2.3 \times 10^{-4} M_{\odot}$.

to a power law $\rho \propto r$. Clumps were distributed stochastically with probability $\propto r^{-8}$ compared to $r^{-2.7}$ in our standard models discussed earlier. Equal numbers of [O I] packets were emitted from each clump. The increased steepness of the density profile is required to compensate for the clumped packet emission relative to the previous smooth distribution. Since the clumps are distributed stochastically according to the density profile, less flux is emitted from the central regions in a clumped emission model than in a smooth distribution model (since there are gaps between the clumps). In order to obtain a sufficiently steeply rising line profile, the density profile must therefore be steepened in clumped emission models. The adopted value of β does not significantly affect the best-fitting values of the other parameters of interest however. Hα was distributed smoothly according to a density power law $\rho(r) \propto r^{-1.3}$. $R_{\rm out}$ was the same for all components (i.e. clumped dust, diffuse dust, [O I] emission and Hα emission) and was calculated using a maximum velocity of 3250 km s^{-1}. The inner radius was $R_{\rm in} = 0.07R_{\rm out}$ for all components except the smooth Hα

emission which was emitted between $R_{\rm in} = 0.25R_{\rm out}$ and $R_{\rm out}$.

The total dust mass used was $M_{\rm dust} = 2.3 \times 10^{-4}$ M$_{\odot}$. This dust mass is very similar to that derived from our original clumped models of [O I] using amorphous carbon grains of radius $a = 0.6\mu$m. The slight increase over our amorphous carbon dust mass of 1.5×10^{-4} M$_{\odot}$ is largely due to the higher grain density of MgSiO$_3$. At this grain radius amorphous carbon and MgSiO$_3$ have similar extinction efficiencies and so the change in species and geometry does not substantially alter the dust mass. We therefore adopt the [O I] dust masses in our further analyses and consider the differences in our derived dust masses between Hα and [O I] to be the result of the clumped emission of [O I].

Fits to both the [O I]λ6300,6363 Å and Hα lines for day 714 using these parameters are presented in Fig. 14.

5.6 The effect of a grain size distribution

It is important to consider the potential effect on the dust mass of modelling a grain size distribution instead of a single grain size. For a grain size distribution the overall extinction cross-section, $C_{\rm ext}$, at a given wavelength is

$$C_{\rm ext} = \int_{a_{\rm min}}^{a_{\rm max}} Q_{\rm ext}(a)n(a)\pi a^2 da \qquad (14)$$

where $Q_{\rm ext}(a)$ is the extinction efficiency for a grain size a and $n(a)$ is the number of grains with size a. The overall extinction efficiency is then

$$Q_{\rm ext} = \frac{C_{\rm ext}}{\int_{a_{\rm min}}^{a_{\rm max}} n(a)\pi a^2 da} \qquad (15)$$

The scattering cross-section $Q_{\rm sca}$ is similarly calculated. As a result of these calculations, there is rarely a single grain size that has the same albedo and extinction efficiency as a size distribution. Modelling a size distribution may therefore alter the deduced dust mass. Since the models are only sensitive to the overall optical depth and albedo, it is not possible to deduce the grain size range or distribution and only single grain sizes are investigated (as presented above).

Whilst this apparently limits the scope of the results, it is useful to consider the extent to which different grain size distributions would alter the derived dust masses. By considering a number of grain radius ranges and adopting a power law distribution with a variable exponent, we may gain some insight into the effects of adopting a distribution rather than a single size. As discussed in Section 5.1, for a classical MRN power law ($n(a) \propto a^{-3.5}$) with a wide grain radius range ($a_{\rm min} = 0.001$ μm to $a_{\rm max} = 4.0$ μm) the derived albedo is much too small to reproduce the required wing seen at early epochs. We therefore adopt an approach whereby, for a number of grain size ranges, we adjust the exponent of the distribution until the overall albedo is the same as that seen for the best fitting single grain radius for the clumped distributions. We may then approximately calculate the required dust mass as

$$M_{\rm d} = \frac{M_{\rm s}Q_{\rm ext,s}(a_s)}{a_{\rm s}} \times \frac{\int_{a_{\rm min}}^{a_{\rm max}} n(a)a^3 da}{\int_{a_{\rm min}}^{a_{\rm max}} Q_{\rm ext}(a)n(a)a^2 da} \qquad (16)$$

Table 9. Dust masses for day 714 clumped models of the Hα line using different grain size distributions and 100% amorphous carbon. The final column shows the factor of increase over the dust mass for the single size model ($M = 7 \times 10^{-5} M_\odot$ with $a = 0.6$ μm) and p is the exponent of the grain size distribution $n(a) \propto a^{-p}$.

$a_{\min}$ (μm)	$a_{\max}$ (μm)	p	M ($M_\odot$)	$M/M_{0.6}$
0.001	4.0	2.45	1.93×10^{-4}	2.76
0.01	4.0	2.45	1.93×10^{-4}	2.76
0.05	4.0	2.52	1.84×10^{-4}	2.62
0.1	4.0	2.72	1.61×10^{-4}	2.3
0.5	4.0	8.20	7.23×10^{-5}	1.03

Table 10. Dust mass conversion factors for single size models using grains of 100% Zubko BE amorphous carbon or 100% Draine & Lee silicate at $\lambda \sim 656$ nm. f is the factor by which the dust mass changes on going from amorphous carbon to silicates.

	carbon			silicates			
a (μm)	ω	Q_{ext}	a (μm)	ω	Q_{ext}	$\text{M}_{\text{sil}}/\text{M}_{\text{amc}}$
0.6	0.56	2.61	0.0583	0.58	0.08	5.37
0.6	0.56	2.61	4.00	0.56	2.18	13.0
3.5	0.62	2.21	0.0641	0.64	0.10	0.65
3.5	0.62	2.21	1.020	0.63	2.15	0.49
3.5	0.62	2.21	1.376	0.62	2.35	0.61

where the subscript s represents the single grain size quantities and the d subscript represents quantities for the grain size distribution.

We calculate the required dust masses for the clumped Hα model on day 714 for a selection of distributions with varying $a_{\min}$. These are presented in Table 9. It can be seen that in all cases, a larger dust mass is required for grain size distributions in order to reproduce the same profile as a single grain size. The conversion factors presented in the table are valid for any model with grain size $a = 0.6$ μm and may therefore also be applied to the models for day 806. We repeated the process for $a = 3.5$ μm but found that, in order to reproduce the required albedo, the distribution had to be heavily weighted towards the larger grains and that the value of $a_{\min}$ had no effect on the required dust mass. Increasing the value of $a_{\min}$ to larger values (> 2 μm) does not have a significant effect either. This is because both extinction efficiency and albedo tend to a constant value with increasing grain radius and the adoption of different grain size ranges and distributions above a certain threshold results in only insignificant variations in these quantities.

We conclude that if a distribution of grain sizes is indeed present, the deduced single size dust masses are likely to under-estimate the true mass of newly formed dust.

5.7 The effect of different grain species

In our analyses so far, we have mostly focused on amorphous carbon as the species of interest. This was motivated by previously published early epoch optical and IR SED analyses that found that the silicate mass fraction must be limited to $\leq 15\%$ (Ercolano et al. (2007), W15). The recent suggestion by Dwek & Arendt (2015) that large masses of the glassy silicate MgSiO$_3$ may have formed at early epochs is discussed further in the next subsection. The parameters that affect the quantity of dust required by our models are the mean albedo and optical depth of the dust. There could be multiple combinations of grain species and sizes that result in a good fit to the data.

We can evaluate the required change in dust mass when a medium of 100% silicates is used instead of amorphous carbon. Using the astronomical silicate optical constants of Draine & Lee (1984), which are 'dirtier' (with lower albedos) than the glassy pure MgSiO$_3$ sample of Jäger et al. (2003). In a similar manner to the approach detailed in Section 5.6, we

can calculate the mass of DL silicate that gives a fit equivalent to that for a single carbon grain radius. We consider the albedo for the grain radius needed for the best-fitting amorphous carbon model, calculate the equivalent grain radius for DL silicate that gives the same albedo and then calculate a new dust mass by allowing for the change in the extinction cross-section:

$$M_{\text{sil}} = M_{\text{amc}} \left(\frac{Q_{\text{amc}}}{Q_{\text{sil}}} \right) \left(\frac{a_{\text{sil}}}{a_{\text{amc}}} \right) \left(\frac{\rho_{\text{sil}}}{\rho_{amC}} \right) \quad (17)$$

Because of the nature of the variation of albedo with grain radius for the Draine & Lee (1984) astronomical silicate (see Fig. 7), there is often more than one silicate grain radius that will give rise to the same albedo at a given wavelength. Some of the possibilities and the resulting mass conversion factors are given in Table 10. For our best fitting amorphous carbon models with $a = 0.6$ μm (the first two entries in Table 10), using any fraction of silicates with either $a = 0.6$ μm or $a = 3.5$ μm would increase the dust mass. However, for the case of an amorphous carbon grain radius of $a = 3.5$ μm (the last three entries), using silicate dust would reduce the dust mass by a factor of about 2 relative to our amorphous carbon values.

5.8 Modelling large masses of dust at early epochs: comparison with the results of Dwek & Arendt (2015)

In a recent analysis of infrared SED data, DA15 suggested that it may be possible for a large mass (0.4M$_\odot$) of MgSiO$_3$ silicate dust to have been present in SN 1987A even at relatively early epochs ($t \sim 615$ d), since that species has very low IR emissivities. Up to this point, we have constructed models using Zubko et al. (1996) BE amorphous carbon dust but in the previous section we discussed the effect on derived dust masses of instead using Draine & Lee (1984) astronomical silicate which has higher optical and IR emissivities than the glassy MgSiO$_3$ species considered by DA15. Our clumping structure in our models was based on that used by W15.

We now consider models for day 714 based on the grain types used by DA15. We adopt a clumped structure equivalent to the preferred model of DA15 who considered 1000 clumps with a filling factor of 0.09 and a negligible dust
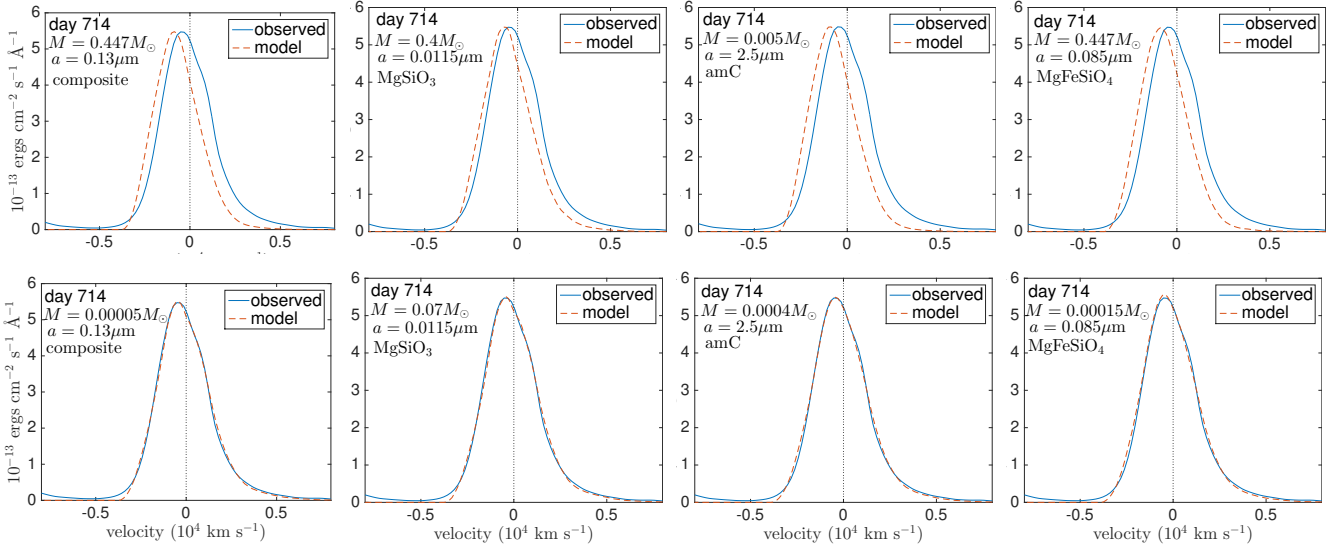
Figure 15. Hα models using different grain species and dust masses. Models for the dust masses presented by Dwek & Arendt (2015) are on the top and models using our minimum required dust masses are on the bottom. From left to right the dust species are composite grains (82% MgSiO$_3$ and 18% amorphous carbon by volume), pure MgSiO$_3$, pure amorphous carbon and pure MgFeSiO$_4$. A density distribution with $\beta = 2.3$ was adopted with a filling factor $f = 0.09$ and an effective clump radius $R_{\rm eff}/R_{\rm out} = 0.044$. All other parameters are the same as in Table 5.

mass in the inter-clump medium. We calculate the effective spherical radius of our clumps by equating the volume of our cubic clumps to a sphere of radius $R_{\rm eff}$. Clumps of width $R_{\rm out}/14$ generate the desired $R_{\rm eff}/R_{\rm out} = 0.044$ equivalent to that of DA15. In our code, using a filling factor of 0.09 then generates 1034 clumps, similar to the number used by DA15. We ran a series of models (presented in Figs 15 and 16) for both the Hα and [O I]λ6300,6363 Å line profiles. In each case we modelled the lines using a dust grain mixture as described by DA15 such that the medium comprised 18% amorphous carbon and 82% MgSiO$_3$ by volume. We adopted the same optical constants as used in their work (i.e. Jäger et al. 2003 for MgSiO$_3$ grains and Zubko et al. 1996 for amorphous carbon) and the same grain mass densities as DA15, $\rho_s = 3.2$ g cm^{-3} and $\rho_c = 1.8$ g cm^{-3}. In addition to modelling their composite grain case, we also considered three single species models, using Zubko BE amorphous carbon, MgSiO$_3$, and MgFeSiO$_4$ (in the latter two cases the optical constants were taken from Jäger et al. 1994 and Dorschner et al. 1995). For each species we adopted the smallest single grain size that has an albedo of $\omega \approx 0.6$. The ejecta parameters were as listed in Table 5, with the exception of the density distribution which we took to be $\rho(r) \propto r^{-1.3}$ for Hα and $\rho(r) \propto r^{-2.3}$ for [O I] in order to optimise the best fits.

For each species, two models are presented. The first adopts the minimum possible dust mass that provides a reasonable fit to the observed line profiles and the second uses the dust mass derived by DA15 for that specific species ($M = 0.4\ M_\odot$ for MgSiO$_3$ and $M = 0.047\ M_\odot$ for amorphous carbon giving a total composite dust mass of $M = 0.447\ M_\odot$). We treated MgFeSiO$_4$ as we do the composite grains and adopted a dust mass of $M = 0.447\ M_\odot$ for it. Results from the models are presented in Figs 15 and 16.

The [O I] models can display similar profiles for substantially different dust masses. This is a result of the relatively high optical depths within the clumps themselves. If a clump is optically thick then the majority of radiation that hits it will be absorbed and the profile becomes insensitive to how much dust is actually contained within the clump. For our [O I] minimum dust mass models, the optical depths within a clump over an effective clump radius $R_{\rm eff}$ at 6300Å are around $\tau_{\rm clump} \approx 0.4$. Over the entire nebula optical depths are very high and $\sim$72% of the total flux is absorbed. Increasing the total dust mass therefore has only a small effect on the emergent line profile and once $\tau_{\rm clump} > 1$ then the line profile remains unchanged for increasingly large dust masses. It is because of this fact that we present only the smallest dust mass capable of reproducing the [O I] profiles seen in Fig. 16. The insensitivity of the [O I] profiles to dust mass is not the case for the Hα profile models (where $\tau_{\rm clump} < 0.05$ for all of our models) and the Hα-fit dust masses presented in Fig. 15 therefore represent the most sensitive diagnostic of the dust mass for each grain type. All of our models discussed in previous sections have significantly smaller clump optical depths ($\tau_{\rm clump} < 0.1$), making them sensitive to dust mass variations.

For all the [O I] line profile models, except for those using pure MgSiO$_3$ or pure Mg$_2$SiO$_4$ dust, the required dust masses are significantly less than those proposed by DA15. The [O I] profile obtained using DA15's very large MgSiO$_3$ dust mass of 0.4 M$_\odot$ provides a reasonable fit, but the same dust mass significantly overestimates the blueshifting of the Hα line (Figure 15). We can place an upper limit on the mass of pure MgSiO$_3$ on day 714 of 0.07 M$_\odot$, as this is the highest mass for which a fit to the observed Hα profile can be obtained (Figure 16).

Pure MgSiO$_3$ is extremely glassy, with very high albedos in the optical for a wide range of grain radii. At grain radii small enough to reduce the albedo to $\omega \approx 0.6$, in order to fit the observed line profiles, the extinction efficiency in the optical becomes extremely low (see Fig. 7),
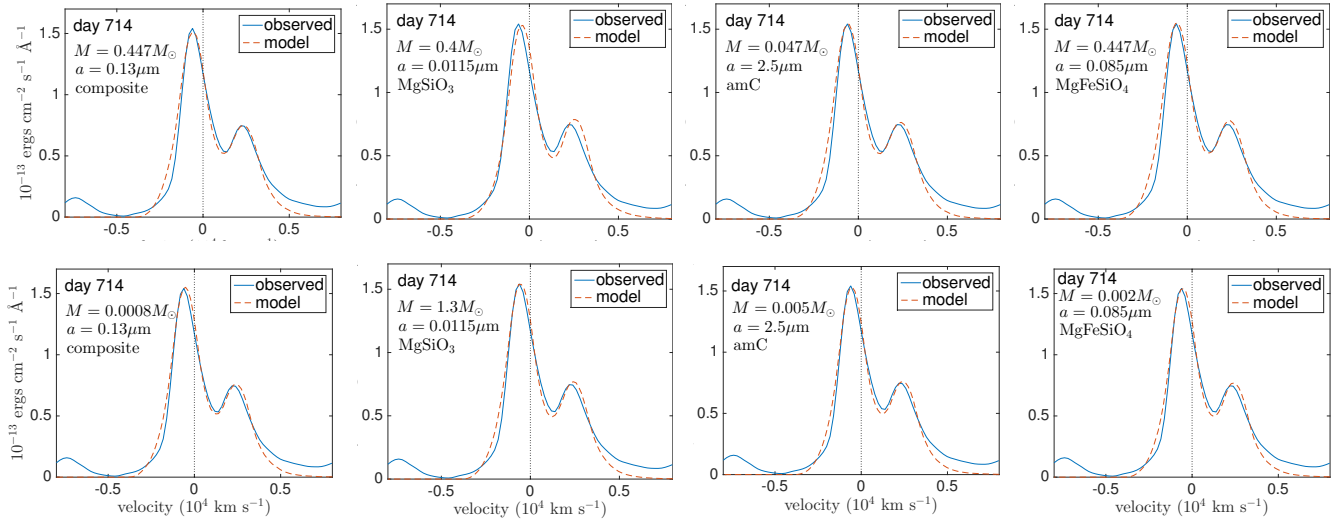
Figure 16. [O I]λ6300,6363 Å models using different grain species and dust masses. Models using the dust masses presented by DA15 are on the top and models using our minimum required dust masses are on the bottom. From left to right the species are composite grains (82% MgSiO$_3$ and 18% amorphous carbon by volume), pure MgSiO$_3$, pure amorphous carbon and pure MgFeSiO$_4$. A density distribution with $\beta = 1.3$ was adopted with a filling factor $f = 0.09$ and an effective clump radius $R_{\rm eff}/R_{\rm out} = 0.044$. The ratio between the doublet components was 2.2. All other parameters are the same as in Table 5.

with large masses of dust therefore required in order to produce even a small amount of line absorption. However, for a given albedo, the extinction efficiencies increase by large factors if either carbon or iron is included in the grain. In the composite grain model the amorphous carbon component dominates the overall extinction due to its much larger extinction efficiency at small grain radii. Similarly, for MgFeSiO$_4$ (or Mg$_{0.5}$Fe$_{0.5}$SiO$_3$) grains the iron component leads to much larger optical and IR extinction efficiencies and much lower dust mass upper limits. If the dust that formed at early epochs contained some fraction of elements such as carbon, iron or aluminium, yielding 'dirtier' silicate grains or composite grains, then fits to the observed blueshifted line profiles imply low dust masses. We conclude that for dust masses as large as 0.07 M$_\odot$ to have been present in SN 1987A's ejecta as early as days 600-1000 then the dust would have to have been formed of glassy pure magnesium silicates.

In order to be certain that there was no set of parameters for which a dust mass of $M = 0.447 M_\odot$ comprising 82% MgSiO$_3$ and 18% amorphous carbon by volume could result in a good fit, a thorough investigation of the variable parameters was performed. Having fixed the clump size, filling factor, dust mass and composition as per the values detailed above and in DA15, we varied the density profile (β) and grain radius a. Varying the maximum velocity and the ratio of the inner and outer radii was found to have little effect on the goodness of fit. The MSE for the Hα profile presented in the upper left panel of Fig. 15 was 0.599 (in units of 10^{-13} erg cm^{-2} s^{-1}). This was improved to 0.246 by increasing the grain radius to $a = 0.6\mu$m and the density profile exponent to $\beta = 1.5$, which represents the best fit that we could achieve using the values described by DA15 and a dust mass of $M = 0.447 M_\odot$. However, the overall best fit we obtain for this scenario (see the lower left panel of 15)

used a dust mass of $M = 5 \times 10^{-4} M_\odot$ giving a MSE=0.0058, substantially improving the fit.

5.9   Unattenuated line fluxes

The evolution of the SN 1987A Hα and [O I]λ6300,6363 Å line fluxes over time has been discussed previously by, for example, Li & McCray (1992), Xu et al. (1992) and Kozma & Fransson (1998b). We may use our clumped models to predict the unattenuated emitted line fluxes and consider their evolution through time. For each model, the fraction of the total line energy absorbed by the dust was predicted. We determined the total flux for each observed line profile and used the absorbed fraction from our clumped models for $a = 3.5\mu$m to predict the undepleted flux of the line before attenuation by the dust. Gaps in the observed data due to contamination by narrow line emission were interpolated over in order to estimate the flux of the broad line component. The observed Hα luminosities and predicted undepleted luminosities are given in Table 3 along with the energy fraction absorbed by the dust in each model. No correction has been made for interstellar extinction along the sightline to SN 1987A. There is very little change in these values if we adopt the models with $a = 0.6$ μm instead of $a = 3.5$ μm. Plots of the observed and undepleted line luminosities are given for all modelled epochs of Hα and [O I] in Figure 17.

We also present power-law fits to the time evolution of the unattenuated Hα and [O I] line fluxes. For Hα, we find that $L_{H\alpha}(t) \propto t^{-4.15}$ between days 714 and 3604. We can compare this value to the theoretical time dependence of the flux of a recombination line based on the dynamics of the ejecta for an environment in a Hubble-type flow $r = vt$. For a frozen-in ionization structure, the mean intensity of a recombination or collisionally-excited line per unit volume is locally proportional to the product of the densi-

ties of the recombining species i.e. $J_{H\alpha} \propto n_e n_p \propto n_e^2$. The total luminosity of the line is therefore dependent on the volume V as $L_{H\alpha} \propto 1/V$. Assuming a constant maximum expansion velocity, the luminosity should vary with time as $L_{H\alpha}(t) \propto t^{-3}$.

This relationship is only true for a constant ionization fraction. This 'freeze-out' phase is estimated to have begun at ~ 800 d and first sets in at lower density high velocity regions, gradually moving inwards with time (Danziger et al. 1991; Fransson & Kozma 1993). Since our modelling begins at day 714, the ionization fraction in the inner higher density regions is likely still decreasing due to recombination during our first two epochs. This presumably accounts for the slightly steeper $L_{H\alpha}(t) \propto t^{-4.15}$ that we find across all epochs. Kozma & Fransson (1998b) estimate that Hα emission from the outer regions begins to dominate over Hα emission from core regions for $t > 900$ d. If earlier epochs are ignored, the last five epochs ($t \geq 1862$ d) plotted in (Fig. 17) exhibit a shallower trend that is in good agreement with the expected $L_{H\alpha}(t) \propto t^{-3}$ evolution.

The [O I]λ6300,6363 Å doublet exhibits a much steeper evolution, $L_{[OI]}(t) \propto t^{-7.2}$, than the H$\alpha$ line (Fig. 17). These collisionally excited lines are very sensitive to the gas temperature, with emissivities that fall to low values for temperatures below $\sim$3000 K. The models of Li & McCray (1992) and Kozma & Fransson (1998a) predict that the gas temperature in the relevant [O I] emitting regions should have fallen below 1000 K after day $\sim$1000.

6 DISCUSSION

Using Monte Carlo models that consider both the absorbing and scattering effects of dust, we have modelled the evolution of the Hα and [O I] λ6300,6363 Å line profiles over time, enabling us to place constraints on the evolution of newly formed dust in the ejecta of SN 1987A.

As can be seen in Fig. 12, even a small degree of asymmetry in observed supernova line profiles can be indicative of dust formation within the ejecta. In addition to this, a line profile that is consistently asymmetric through time requires increasingly large dust masses to account for a similar degree of blueshifting since the expansion of the ejecta would otherwise cause the dust optical depth to the edge of the ejecta to be reduced.

In Section 5.8 we compared our results with those of Dwek & Arendt (2015) and concluded that large dust masses can only have been present at early epochs if the grains were formed purely of glassy magnesium silicates that contained no iron or carbon component and that even for pure magnesium silicates no more than 0.07 M$_\odot$ could have been present. We now compare our results with those of Lucy et al. (1989) and W15.

Lucy et al. (1989) analysed the [O I] λ6300,6363 Å doublet for SN 1987A and estimated dust optical depths for a number of epochs. They translated these into dust masses for day 775 only. From our smooth flow modelling of the [O I] doublets, we obtain $\tau_V \approx 3.60$ at day 714 and $\tau_V \approx 2.86$ at day 806. These values are higher than the values given by Lucy et al. (1989) who derived $\tau_V = 1.19$ at day 725 and $\tau_V = 1.25$ at day 775. The value of the assumed albedo accounts for the majority of this discrepancy. Lucy et al. (1989)
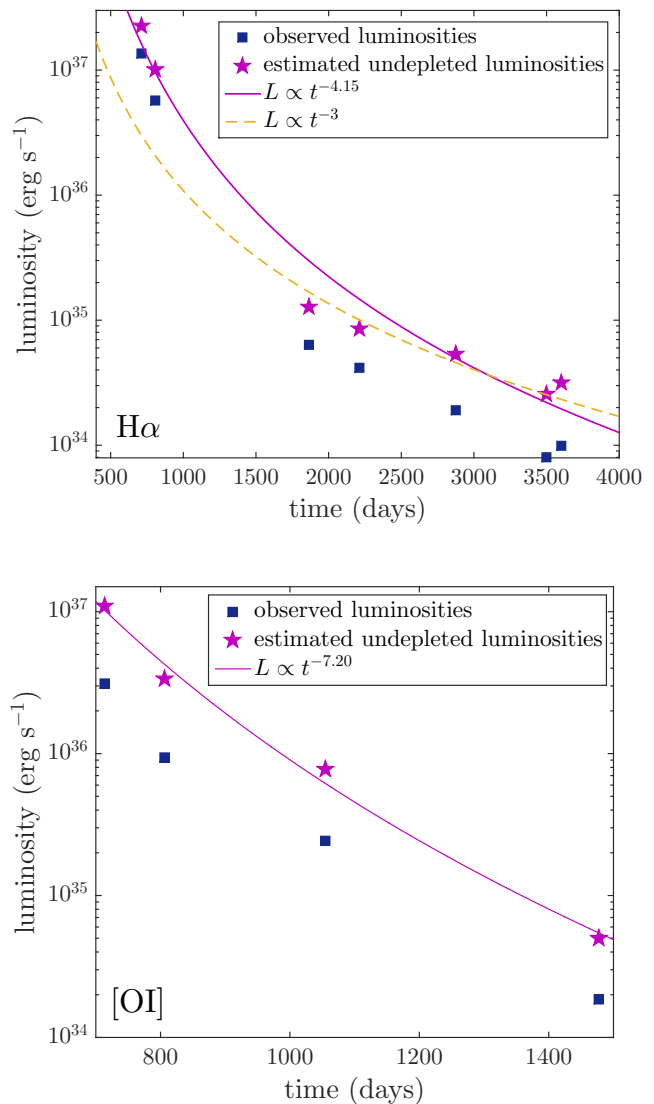

Figure 17. Predicted undepleted luminosities for the Hα line (above) and [O I]λ6300,6363 Å doublet (below) presented with the best power-law fit to the data.

considered line profiles before and after dust condensation and concluded that any evidence of an extended red scattering wing was unconvincing. Accordingly, they adopted a model with perfectly absorbing dust ($\omega = 0$). For our amorphous carbon models for the [O I] $\lambda\lambda$6300,6363 Å profile using a grain radius $a = 0.35\mu$m, we obtain an albedo of approximately $\omega = 0.5$ at $\lambda = 6300$ Å.

The dust masses derived by Lucy et al. (1989) at day 775 (e.g. $M_{dust} = 4.4 \times 10^{-6} M_\odot$ for amorphous carbon) are different to those obtained from our smooth dust modelling of the [O I] $\lambda\lambda$6300,6363 Å doublet at day 806 ($M_{dust} = 1.5 \times 10^{-4} M_\odot$ for amorphous carbon). There are three main reasons for the discrepancy. First, the albedo is significantly larger in our modelling as already discussed. A larger dust mass is therefore required to produce the same amount of absorption. Secondly, to match the extended red wing our required grain radius is considerably larger than the small
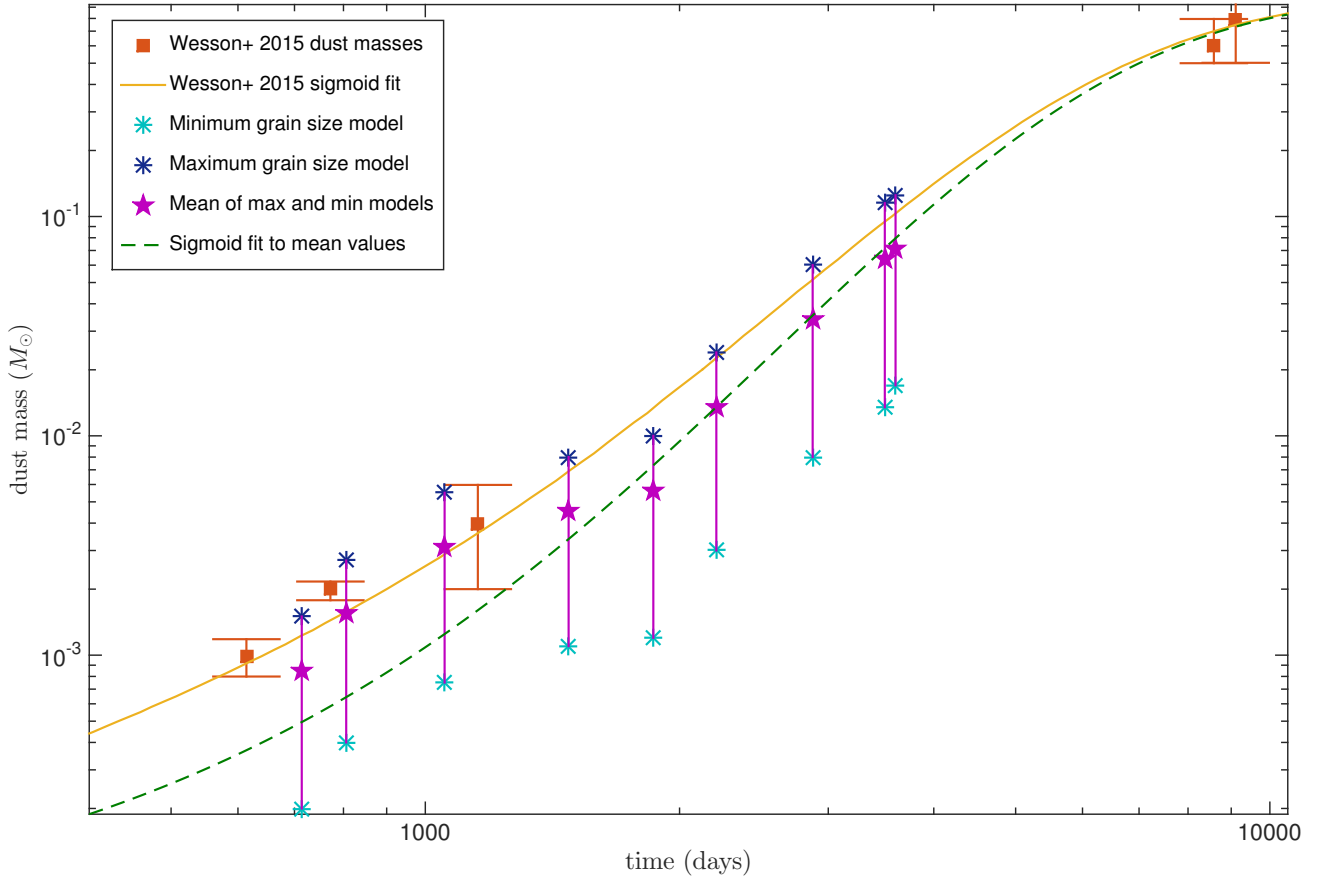
Figure 18. Derived dust masses for SN 1987A as a function of epoch. *Red squares* - dust masses derived by W15 from their photometric SED modelling of SN 1987A. *Solid yellow line* - W15's sigmoid fit to their values. *Dark and light blue asterisks* - maximum ($a = 3.5$ μm) and minimum ($a = 0.6$ μm) dust masses respectively for the [O I] models for $t \leq 1478$ days and for the Hα models for $t \geq 1862$ days. *Purple stars* - predicted dust masses calculated as the mean of the maximum and minimum dust masses. *Dashed green line* - sigmoid fit to our predicted dust masses.

grains ($a < 0.1\mu$m) adopted by Lucy et al. (1989). Larger grain radii reduce the total cross-section of interaction and so a greater dust mass must be present to compensate for this. Finally, the adopted maximum velocity (4000 km s^{-1}) in our model is larger than the value adopted by Lucy et al. (1989, 1870 km s^{-1}). The larger value of V_{max} increases the total volume of the ejecta significantly and therefore significantly more dust is required to produce the same optical depth.

Lucy et al. (1989) also noted that the dust optical depth increased rapidly after day 580 and that the rate of increase of the dust optical depth appeared to slow between day 670 and day 775, the latest day that they considered. Our results, for both clumped and smooth models, suggest that the dust optical depth actually drops between day 714 and day 806 before starting to increase again at later epochs. This is consistent with the results of Lucy et al. (1989) where the slowing rate of increase of dust optical depth could be consistent with a turning point subsequent to day 775.

We can also compare our dust masses with the mass estimates derived from SED-fitting by W15 (see Fig. 18).

W15 used a sigmoid fit to their dust mass evolution, of the form

$$M_d(t) = ae^{be^{ct}}, \qquad (18)$$

where $a = 1.0M_\odot$ (representing the limiting dust mass), $b = -8.53$ and $c = -0.0004$. Both their dust masses and this sigmoid fit are shown in Fig. 18. It exhibits an initial period of slow growth in mass followed by an intermediate period of accelerating growth followed by another slowing until a plateau is ultimately reached. In this sense it may be representative of the process of dust formation whereby initial conditions appropriate for grain growth gradually develop until optimal conditions are reached at an intermediate epoch when grain growth is at its fastest before conditions once again deteriorate and the rate slows again (as discussed by W15). Performing a least-squares regression to this function using just our own derived clumped dust masses, we obtain a sigmoid fit with coefficients $a = 1.0M_\odot$, $b = -10.0$ and $c = -0.0004$. These values are remarkably similar to those derived by W15. This sigmoid fit is also plotted in Fig. 18.

We find that at all epochs the dust masses derived by W15 are entirely within the dust mass ranges determined by our models.

Our sigmoid fit to the mean of the maximum and minimum dust masses does not take into account any systematic effects of grain growth. At earlier epochs, whilst grains are still small relative to later epochs, the lower bound to the dust mass estimates may be more representative than the upper end; the reverse would be true at later epochs. This is in contrast to the sigmoid fit of W15, whose fits to their early epoch SEDs used an MRN distribution with grain radii between 0.005 and 0.25 μm, whilst their fits to their last two epochs required grain radii between 3.005 and 3.25 μm. The dust masses used for their sigmoid fit thus accounted for the effects of grain growth between the earlier and later epochs. As mentioned, we could not fit the extended red wings of the profiles at early epochs using an MRN distribution. W15 found that at their earlier epochs they could not obtain SED fits with grain radii as large as ~ 1.0 μm. However, they did not consider radii in between these size ranges, such as the grains with $a \approx 0.6$ μm that we require at earlier epochs. For SED modelling it is generally the case that the larger the grain size used, the less dust is required to produce the same level of flux. This may account for the differences between W15's earlier epoch dust masses and our own minimum dust mass estimates at similar epochs. The models of W15 used 15% silicate dust, in contrast to our models which used 100% amorphous carbon dust. This could also contribute to the differences at early epochs, as could the use of different sets of optical constants – we used the BE amorphous carbon optical constants of Zubko et al. (1996) whereas W15 used AC constants from Hanner (1988). W15 found that in order to fit early epoch SEDs epochs (e.g. day 615) with Zubko ACH2 constants, smaller inner and outer ejecta radii were needed, with half as much dust ($5.0 \times 10^{-4} M_\odot$) compared to the Hanner AC results.

W15 derived a maximum possible grain size at late epochs, concluding that the grains could not be larger than ~ 5 μm by day 8515. This is consistent with the maximum grain radii that we derive at our latest epochs. We find that grain radii most likely cannot have exceeded ~ 3.5 μm at day 3604 - the dust mass that we obtain using this grain radius is similar to the value predicted by W15's sigmoid fit at that epoch.

The relationship between ejecta dust grain radii and post-explosion time is important for understanding the likelihood of dust surviving the passage of a reverse shock propagating back through the ejecta. By the time the effects of a reverse shock begin to appear in the line profiles (around day 5000), our models imply that the grains could already be as large as several microns in radius and are likely to be larger than ~ 0.6 μm. Grains as large as this are more likely to survive destruction by sputtering in supernova reverse shocks and in interstellar shocks (Silvia et al. 2010, 2012; Slavin et al. 2015). It has been suggested that very large grains (radii up to 4.2 μm) formed in the ejecta of SN 2010jl within a few hundred days after the explosion (Gall et al. 2014). The grain radii that W15 and ourselves obtain for SN 1987A at very late epochs are nearly as large as found by Gall et al. (2014) for SN 2010jl, with both results suggesting that grains large enough to survive the destructive

force of a reverse shock have formed by a few hundred days post-explosion.

The dust masses obtained from our modelling of SN 1987A's line profiles support the conclusion of W15 that even after ~ 3000 d the dust mass was still only a fraction of its current value. This contrasts with the results of Sarangi & Cherchneff (2015) whose grain chemistry models predict that ejecta dust masses should plateau by around 5 yr after the explosion. Our results show that SN 1987A's dust mass had reached of the order of $0.1 M_\odot$ by day 3604. Since its present dust mass is several times larger than this (Matsuura et al. 2015, W15), a substantial fraction of the current dust mass must have condensed after this epoch, in agreement with the conclusions of W15.

Ideally, our models would cover the entire evolution of SN 1987A's Hα line profiles up to the present day. However, the excitation of gas in the outer edges of the ejecta by the reverse shock after $\sim$ day 5000 results in significant broad and asymmetric emission that dominates the original line profile (Fransson et al. 2013). In addition to this, the narrow lines from the equatorial ring start to become so strong relative to the declining broad Hα profile that, post-removal, not enough of the broad profile remained to be able to reliably infer information from the profile structure. These factors may be common to some other CCSNe that have interactions with surrounding circumstellar material. Care should also be taken to ensure that any observed late-time line profiles being modelled are not in fact the product of a light echo reflecting the spectrum from near maximum light. Nonetheless, detailed line modelling of asymmetric line profiles has proved effective in determining dust masses in the ejecta of SN 1987A at multiple epochs during the first ten years after outburst. The method clearly has wider application to other supernovae.

7 CONCLUSIONS

We have investigated the effects of scattering and absorption by ejecta dust on supernova line profile shapes and the different characteristic features that may be produced. In particular, attention is drawn to the fact that a classical blueshifted peak and asymmetric profile with most flux on the blue side is not the only profile type that can signify the presence of dust. In the case of strong dust scattering, line profiles can have the majority of their flux on the red side. Even with just some dust scattering, profiles can often exhibit an extended red scattering wing, although care should be taken to ascertain that this cannot be accounted for by electron scattering (electron scattering optical depths should usually only be significant at very early epochs, < 200 d). The line peak should always lie on the blue side, with a line peak velocity that will often correspond to the minimum velocity at the inner edge of the ejecta shell. If not obscured by narrow circumstellar [N II] 6584 Å emission, a pronounced shoulder or corner may be present on the red side of the profile, also corresponding to the minimum velocity at the inner edge of the ejecta shell.

We have modelled the Hα and [O I] λ6300,6363 Å line profiles from SN 1987A over a range of epochs and have obtained dust masses of the order of $0.1 M_\odot$ by day 3604. We derive a sigmoid fit to our dust mass data that predicts

a current dust mass of $0.68 M_\odot$, in line with current SED-based dust mass estimates for SN 1987A. We find that large grains are necessary in order to reproduce both the extended red scattering wings and the asymmetry seen in several of the lines and that grains larger than 0.6 μm have formed by day 714, while by day 3604 grain radii of ~ 3.5 μm are needed. We find from fits to the Hα profile that dust masses cannot have exceeded a few$\times 10^{-3}$ M$_\odot$ on day 714 for all the grain types investigated, apart from glassy pure magnesium silicate grains, for which up to 0.07 M$_\odot$ can be fitted.

The observed red-blue line asymmetries persist right through to day 3604 and beyond – if no further dust had formed after day $\sim$800 then the expansion of the ejecta dust shell would cause dust optical depths to drop rapidly with time thereafter, leading to the disappearance of red-blue asymmetries. Just to maintain the observed degree of red-blue asymmetry seen at the earlier epochs therefore requires that dust must have continued to form beyond those epochs.

ACKNOWLEDGEMENTS

REFERENCES

Andrews J. E., et al., 2010, ApJ, 715, 541
Barlow M. J., et al., 2010, A&A, 518, L138
Baron E., Nugent P. E., Branch D., Hauschildt P. H., 2005, in Turatto M., Benetti S., Zampieri L., Shea W., eds, ASP Conf. Ser. Vol. 342, Supernovae as Cosmological Lighthouses. p. 351 (arXiv:astro-ph/0409659)
Bertoldi F., Carilli C. L., Cox P., Fan X., Strauss M. a., Beelen A., Omont A., Zylka R., 2003, A&A, 406, L55
Bouchet P., Danziger I. J., Lucy L. B., 1991, AJ, 102, 1135
Chugai N. N., Chevalier R. a., Kirshner R. P., Challis P. M., 1997, ApJ, 483, 925
Danziger I. J., Bouchet P., Gouiffes C., Lucy L. B., 1991, in Danziger I. J., Kjaer K., eds, Vol. 37, European Southern Observatory Conference and Workshop Proceedings. p. 217
Dorschner J., Begemann B., Henning T., Jaeger C., Mutschke H., 1995, A&A, 300, 503
Draine B. T., Lee H. M., 1984, ApJ, 285, 89
Dwek E., Arendt R. G., 2015, ApJ, 810, 75
Dwek E., Galliano F., Jones A. P., 2007, ApJ, 662, 927
Ercolano B., Barlow M. J., Sugerman B. E. K., 2007, MNRAS, 375, 753
Fabbri J., et al., 2011, MNRAS, 418, 1285
Fransson C., Kozma C., 1993, ApJ, 408, L25
Fransson C., et al., 2013, ApJ, 768, 88
Fransson C., et al., 2014, ApJ, 797, 118
Gall C., et al., 2014, Nature, 511, 326
Gerasimovic B., 1933, Z. Astrophys., 7, 335
Gomez H. L., et al., 2012, MNRAS, 420, 3557
Gröningsson P., Fransson C., Lundqvist P., Nymark T., Lundqvist N., Chevalier R., Leibundgut B., Spyromilio J., 2006, A&A, 5325, 11
Gröningsson P., et al., 2007, A&A, 491, 19
Gröningsson P., et al., 2008, A&A, 479, 761
Hammer N. J., Janka H.-T., Müller E., 2010, ApJ, 714, 1371
Hanner M. S., 1988, NASA Conf. Publ., 3004, NASA, Washington DC
Hanuschik R. W., Spyromilio J., Stathakis R., Kimeswenger S., Gochermann J., Seidensticker K. J., Meurer G., 1993, MNRAS, 261, 909
Henyey L. G., Greenstein J. L., 1941, ApJ, 93, 70
Hillier D. J., 1991, A&A, 247, 455
Hoyle F., Wickramasinghe N. C., 1970, Nature, 226, 62
Indebetouw R., et al., 2014, ApJ, 782, L2
Jäger C., Mutschke H., Begemann B., Dorschner J., Henning T., 1994, A&A, 292, 641
Jäger C., Dorshner J., Mutschke H., Posch T., Henning T., 2003, A&A, 408, 193
Jerkstrand A., Fransson C., Maguire K., Smartt S., Ergon M., Spyromilio J., 2012, A&A, 546, A28
Kotak R., et al., 2009, ApJ, 704, 306
Kozasa T., Hasegawa H., Nomoto K., 1991, A&A, 249, 474
Kozma C., Fransson C., 1998a, ApJ, 496, 946
Kozma C., Fransson C., 1998b, ApJ, 497, 431
Li H., McCray R., 1992, ApJ, 387, 309
Lucy L., 2005, A&A, 429, 19
Lucy L. B., Danziger I. J., Gouiffes C., Bouchet P., 1989, in Tenorio-Tagle G., Moles M., Melnick J., eds, Lecture Notes in Physics, Berlin Springer Verlag Vol. 350, IAU Colloq. 120: Structure and Dynamics of the Interstellar Medium. p. 164, doi:10.1007/BFb0114861
Lucy L., Danziger I. J., Gouiffes C., Bouchet P., 1991, in Woosley S. E., ed., Supernovae. Springer-Verlag, New York, p. 82
Maeda K., Mazzali P. a., Deng J., Nomoto K., Yoshii Y., Tomita H., Kobayashi Y., 2003, ApJ, 593, 931
Mathis J. S., Rumpl W., Nordsieck K. H., 1977, ApJ, 217, 425
Matsuura M., et al., 2011, Science, 333, 1258
Matsuura M., et al., 2015, ApJ, 800, 50
Mauerhan J., Smith N., 2012, MNRAS, 424, 2659
McCray R., 1996, in Kuhn T. S., ed., IAU Colloq. 145: Supernovae and Supernova Remnants. p. 223
Meikle W. P. S., et al., 2007, ApJ, 665, 608
Milisavljevic D., Fesen R. A., Chevalier R. A., Kirshner R. P., Challis P., Turatto M., 2012, ApJ, 751, 25
Morgan H. L., Edmunds M. G., 2003, MNRAS, 343, 427
Omont A., Cox P., Bertoldi F., McMahon R. G., Carilli C., Isaak K. G., 2001, A&A, 374, 371
Owen P. J., Barlow M. J., 2015, ApJ, 801, 141
Phillips M. M., Hamuy M., Heathcote S. R., Suntzeff N. B., Kirhakos S., 1990, AJ, 99, 1133
Roche P. F., Aitken D. K., Smith C. H., James S. D., 1989, Nature, 337, 533
Sarangi A., Cherchneff I., 2015, A&A, 575, A95
Silvia D. W., Smith B. D., Michael Shull J., 2010, ApJ, 715, 1575
Silvia D. W., Smith B. D., Shull J. M., 2012, ApJ, 748, 12
Slavin J. D., Dwek E., Jones A. P., 2015, ApJ, 803, 7
Smith N., Silverman J. M., Filippenko A. V., Cooper M. C.,

Matheson T., Bian F., Weiner B. J., Comerford J. M., 2012, AJ, 17, 6

Spyromilio J., Stathakis R., Cannon R., Waterman L., Couch W., Dopita M., 1991, MNRAS, 248, 465

Spyromilio J., Stathakis R. a., Meurer G. R., 1993, MNRAS, 263, 530

Storey P. J., Zeippen C. J., 2000, MNRAS, 312, 813

Sugerman B. E. K., et al., 2006, Science, 313, 196

Suntzeff N. B., Phillips M. M., Depoy D. L., Elias J. H., Walker A. R., 1991, AJ, 102, 1118

Todini P., Ferrara A., 2001, MNRAS, 325, 726

Tziamtzis a., Lundqvist P., Groningsson P., Nasoudi-Shoar S., 2010, A&A, 35, 15

Wang L., et al., 1996, ApJ, 466, 998

Watson D., Christensen L., Knudsen K. K., Richard J., Gallazzi A., Michaowski M. J., 2015, Nature, 519, 327

Wesson R., Barlow M. J., Matsuura M., Ercolano B., 2015, MN-RAS, 446, 2089 (W15)

Wongwathanarat A., Müller E., Janka H.-T., 2015, A&A, 577, A48

Wooden D. H., Rank D. M., Bregman J. D., Witteborn F. C., Tielens A. G. G. M., Cohen M., Pinto P. A., Axelrod T. S., 1993, ApJS, 88, 477

Xu Y., McCray R., Oliva E., Randich S., 1992, ApJ, 386, 181

Zubko V. G., Mennella V., Colangeli L., Bussoletti E., 1996, MN-RAS, 282, L1321

APPENDIX A: THE LORENTZ TRANSFORM FORMALISM

Since the outflow velocities in supernovae are high, the photon packets are subject to Doppler shifting upon emission and at each scattering event. When the packet is initially emitted, it has a frequency and a trajectory in the rest frame of the emitter. Both of these must be transformed to the observer's frame in order for the packet to be propagated through the grid. The new direction and frequency in the observer's frame may be simply found by transforming the momentum four-vector $\boldsymbol{P}$ which is defined as

$$\boldsymbol{P} = \begin{pmatrix} E \\ p_x \\ p_y \\ p_z \end{pmatrix} = \begin{pmatrix} h\nu \\ h\nu x \\ h\nu y \\ h\nu z \end{pmatrix} \quad \text{(A1)}$$

We may then derive $\boldsymbol{P}'$, the momentum 4-vector in the observer's frame using the relation

$$\boldsymbol{P}' = \Lambda \boldsymbol{P} \quad \text{(A2)}$$

where

$$\Lambda = \begin{pmatrix} \gamma & -\gamma\beta_x & -\gamma\beta_y & -\gamma\beta_z \\ -\gamma\beta_x & 1 + (\gamma-1)\frac{\beta_x^2}{\beta^2} & (\gamma-1)\frac{\beta_x\beta_y}{\beta^2} & (\gamma-1)\frac{\beta_x\beta_z}{\beta^2} \\ -\gamma\beta_y & (\gamma-1)\frac{\beta_y\beta_x}{\beta^2} & 1 + (\gamma-1)\frac{\beta_y^2}{\beta^2} & (\gamma-1)\frac{\beta_y\beta_z}{\beta^2} \\ -\gamma\beta_z & (\gamma-1)\frac{\beta_z\beta_x}{\beta^2} & (\gamma-1)\frac{\beta_z\beta_y}{\beta^2} & 1 + (\gamma-1)\frac{\beta_z^2}{\beta^2} \end{pmatrix}$$

and $\boldsymbol{\beta} = \frac{\mathbf{v}}{c} = (\beta_x, \beta_y, \beta_z)$, $\beta = |\boldsymbol{\beta}|$ and $\gamma = \frac{1}{\sqrt{1-\beta^2}}$.

In practice, the velocities considered are low enough

that it is unnecessary to consider terms of the order of $O(\frac{v^2}{c^2})$ and thus Λ may be reduced to

$$\Lambda = \begin{pmatrix} 1 & -\beta_x & -\beta_y & -\beta_z \\ -\beta_x & 1 & 0 & 0 \\ -\beta_y & 0 & 1 & 0 \\ -\beta_z & 0 & 0 & 1 \end{pmatrix} \quad \text{(A3)}$$

The new direction of travel and frequency in the observer's frame are therefore given by

$$\nu' = \nu(1 - x\beta_x - y\beta_y - z\beta_z) \quad \text{(A4)}$$

$$x' = \frac{\nu}{\nu'}(x - \beta_x)$$

$$y' = \frac{\nu}{\nu'}(x - \beta_y)$$

$$z' = \frac{\nu}{\nu'}(x - \beta_z)$$

For each scattering event, the packet must be transformed both into and out of the comoving frame. The reverse transform is applied by using the inverse Lorentz matrix Λ^{-1} which is obtained by reversing the sign of $\boldsymbol{v}$. Positive $\boldsymbol{v}$ is defined for frames moving away from each other and thus $\boldsymbol{v}$ is defined to be negative in the direction of the observer.

This paper has been typeset from a TeX/LaTeX file prepared by the author.